REVIEW

Check for updates

Reduced graphene oxide today

Raluca Tarcan,[ab] Otto Todor-Boer,[abc] Ioan Petrovai,[ab] Cosmin Leordean,[d] Simion Astilean [ID][ab] and Ioan Botiz [ID] *[a]

Reduced graphene oxide has similar mechanical, optoelectronic or conductive properties to pristine graphene because it possesses a heterogeneous structure comprised of a graphene-like basal plane that is additionally decorated with structural defects and populated with areas containing oxidized chemical groups. The graphene-like properties make reduced graphene oxide a highly desirable material to be used in a plethora of sensorial, biological, environmental or catalytic applications as well as optoelectronic and storage devices. To further advance the development of the existent technologies and to design novel and better applications based on reduced graphene oxide, it is first necessary to understand which synthetic routes and processing strategies are suitable to significantly boost specific properties of this material alone or as a component in various composites. Therefore, in this work, we review the most important categories of recent applications based on reduced graphene oxide, with the emphasis on the relationship between the enhanced composite/device functionality and methods used to synthesize, to functionalize and/or to process and to structure reduced graphene oxide.

Introduction

Carbon atoms are the constituent parts of all allotropic carbonic materials. Carbon is viewed as a versatile material component not only because it is light, but also because it can adopt a variety of configurations with different bonding possibilities that lead to carbon allotropes exhibiting distinct properties. One of the best known carbonic materials is graphene, along with its derivatives graphene oxide (GO) and reduced graphene oxide (RGO).

Graphene is a two-dimensional (2D) crystal made of a basal monolayer of sp[2] hybridized carbon atoms disposed in hexagonal packing, which was theoretically predicted a long time ago[1] and produced only in 2004.[2] It is a building block of many other carbonic materials such as fullerene buckyballs, carbon nanotubes or 3D graphite.[3] Its unique structure leads to astonishing mechanical properties resulting from strong planar σ bonds,[4] as well as impressive electrical properties[5] that arise from π bonds. Graphene is considered the thinnest stretchable crystal possessing good thermal conductivity and high electron mobility.[6] It quickly became essential in a wide range of applications such as optoelectronic devices,[7] sensors,[8] biomaterials and bionics,[9]

energy storage[10] and batteries,[11] electrochemical performance,[12] thermal management,[13] armor material,[14] cigarettes,[15] etc.

There are a variety of top-down methods (repeated peeling,[2] sonication,[16] ball milling,[17] exfoliation,[18] etc.) and bottom-up methods (chemical vapor deposition,[19] silicon evaporation,[20] epitaxial growth,[21] unzipping multiwalled carbon nanotubes,[22] using an electric arc,[23] etc.) to produce graphene. However, despite the fact that significant advances are currently made,[24] production of cheap high-quality graphene at an industrial scale and in large-areas remains a tremendous challenge. That is because many of the above top-down techniques are limited to liquid medium for graphene stabilization, to solvent removal and to very low yields of graphene, which often contains defects. Meanwhile, bottom-up techniques need expensive equipment, the synthesis is performed at high temperatures and it is rather limited to specific metallic substrates on which high quality graphene, yet in limited quantities, is grown. Transferring graphene from, for example, copper to other substrates that are more suitable for various applications is possible,[19] but the process remains challenging and complex as graphene transfer onto flat substrates necessitates avoidance of wrinkles, cracks or broken graphene regions.

Instead, GO can be produced in desirable quantities rather rapidly and at low cost. GO has a 2D structure like graphene but the single-layer of carbon atoms is covalently functionalized with oxygen containing groups (hydroxyl, epoxide, carbonyl, etc.) on the basal plane and on the edges introduced during chemical exfoliation of graphite flakes. These functional groups allow GO to be processed easily in dispersions and confer on it

[a] Interdisciplinary Research Institute in Bio-Nano-Sciences, Babes-Bolyai University, Treboniu Laurian 42, Cluj-Napoca 400271, Romania.
E-mail: ioan.botiz@ubbcluj.ro
[b] Faculty of Physics, Babes-Bolyai University, M. Kogalniceanu Str. 1, 400084, Cluj-Napoca, Romania
[c] INCDO-INOE 2000, Research Institute for Analytical Instrumentation, Donath Street 67, 400293 Cluj-Napoca, Romania
[d] Robert Bosch SRL, Robert Bosch nr. 1, Jucu 407352, Romania

both high colloidal stability in water and a unique set of mechanical, colloidal or optical properties. These GO properties can be further tuned using chemical engineering[25] and can lead to a plethora of applications[26] including solar cells,[27] sensors,[28] supercapacitors,[29] generation of neurons,[30] cellular migration,[31] drug delivery,[32] membranes,[33] multifunctional gels,[34] water purification[35] and many more. High-quality GO can be rapidly produced in dispersions from graphite flakes using well-established chemical[36–38] or electrochemical[39,40] exfoliation methodologies based on protocols proposed by Hummers,[36] Staudenmaier,[37] Brodie[38] or, more recently, other researchers.[40,41] Unfortunately, because most of these methods use strong oxidants, such as potassium permanganate, GO presents significant amounts of defects in its crystalline network. Therefore, GO's conductive properties are far below those of graphene, although its optical and mechanical properties suffer a lesser impact.

Fortunately, GO can regain graphene-like properties by additional reductive exfoliation treatments[42,43] that transform GO into RGO. At this point, RGO is becoming a very good compromise between graphene and GO. This is not only because RGO exhibits graphene-like properties, including relatively good conductivity, but also because RGO is easy to prepare in desired quantities from cheap GO by using a variety of (electro)chemical[44,45] and microwave-[46] and photo-assisted[47] thermal[48] methods. Production of RGO can be further realized using seriography-guided reduction[49] or radiation-induced reduction[50] or solar mediated reduction[51] or even multi-step combined method assisted reduction.[52] Here, it is important to understand that this diversity of reduction processes will lead to different quality RGO with (highly) altered properties, depending on the degree of reduction. For example, chemical reduction is cheap and easy as it can be performed at room temperature or under rather average heating conditions. Generally, this method relies on the use of chemical reagents such as hydrazine and its derivatives hydrazine hydrate and dimethylhydrazine. In these cases, reduction of GO to RGO sheets is achieved through the use of hydrophobicity by simply adding these liquid reagents to a GO aqueous dispersion.[53] Other reagents including sodium borohydride (a good agent that efficiently reduces C=O groups[54]), a combination of sodium borohydride and concentrated sulfuric acid (reduction of GO is improved by an additional dehydration process[52]), hydroiodic acid,[55] ascorbic acid,[56] *etc.* can also be used. Chemical reagents can be completely eliminated when employing the electrochemical method. In this case, the reduction process relies on the GO-electrode electron exchange and it can be performed inside an electrochemical cell in the presence of an aqueous buffer solution. Instead, thermal reduction is based on rapid annealing at high temperatures, which induces exfoliation of graphite/graphene oxide through the expansion of CO or CO_2 gas resulting from the removal of oxygen functional groups. In thermal reduction, in order to obtain high quality RGO with, for example, good conductive properties, it is indicated to use temperatures as high as 1100 °C.[57] Microwave- and photo-assisted procedures[58,59] are further used to assist the thermal reduction method as they present the advantage of rapid and uniform heating of substances using microwave ovens and photo-irradiation with various lasers.
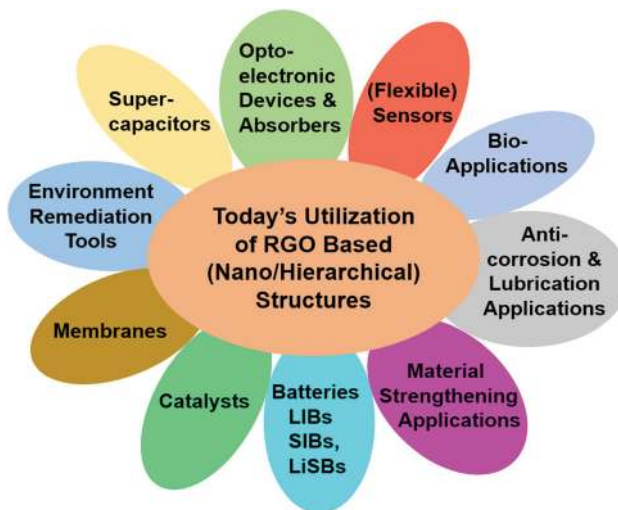
Scheme 1   Summary of various RGO based applications.

Additionally, RGO exhibits not only good absorption properties over the whole spectrum (even a single-layer of RGO can absorb a significant amount of light in the visible and near infrared range[60–63]), but it also possesses functional groups that could make it dispersible in a variety of solvents of interest (it is worth noting that RGO tends to aggregate during the reduction process and therefore much research is dedicated not only to reduction but also to stabilization of RGO using various methodologies[64–73]). As we will further see in this work, these amazing graphene-like properties of RGO have been recently exploited in a plethora of (hierarchically) assembled structures that were incorporated in innovative applications within a wide range of science and technology branches (Scheme 1).

RGO based structures used in fabrication of sensors

Nowadays, detection of specific substances, molecules or atoms at low concentrations is absolutely necessary not only when we are referring to our daily comfort and safety, but also when we are looking towards our more and more polluted environment. Sensors are technological devices that allow us to detect specific unwanted and/or toxic gases in our houses or environment, various life harming biological substances in our food and body or even poisonous substances in soil, water or air. Because the complexity of harmful substances is expanding from day to day and more and more traces of biological substances need to be detected, highly sensitive sensors of better performance need to be continuously designed and developed. Of course, sensors are more attractive when they also are wearable, flexible, transparent, multifunctional, miniaturized, *etc.* From this point of view, RGO is a good candidate for fabrication of sensors and recent examples of RGO based sensor developments reported in the literature are abounding in variety and novelty.

A first important aspect in detection technology is sensing various gases/molecules (including oxygen,[74] carbon monoxide[75]
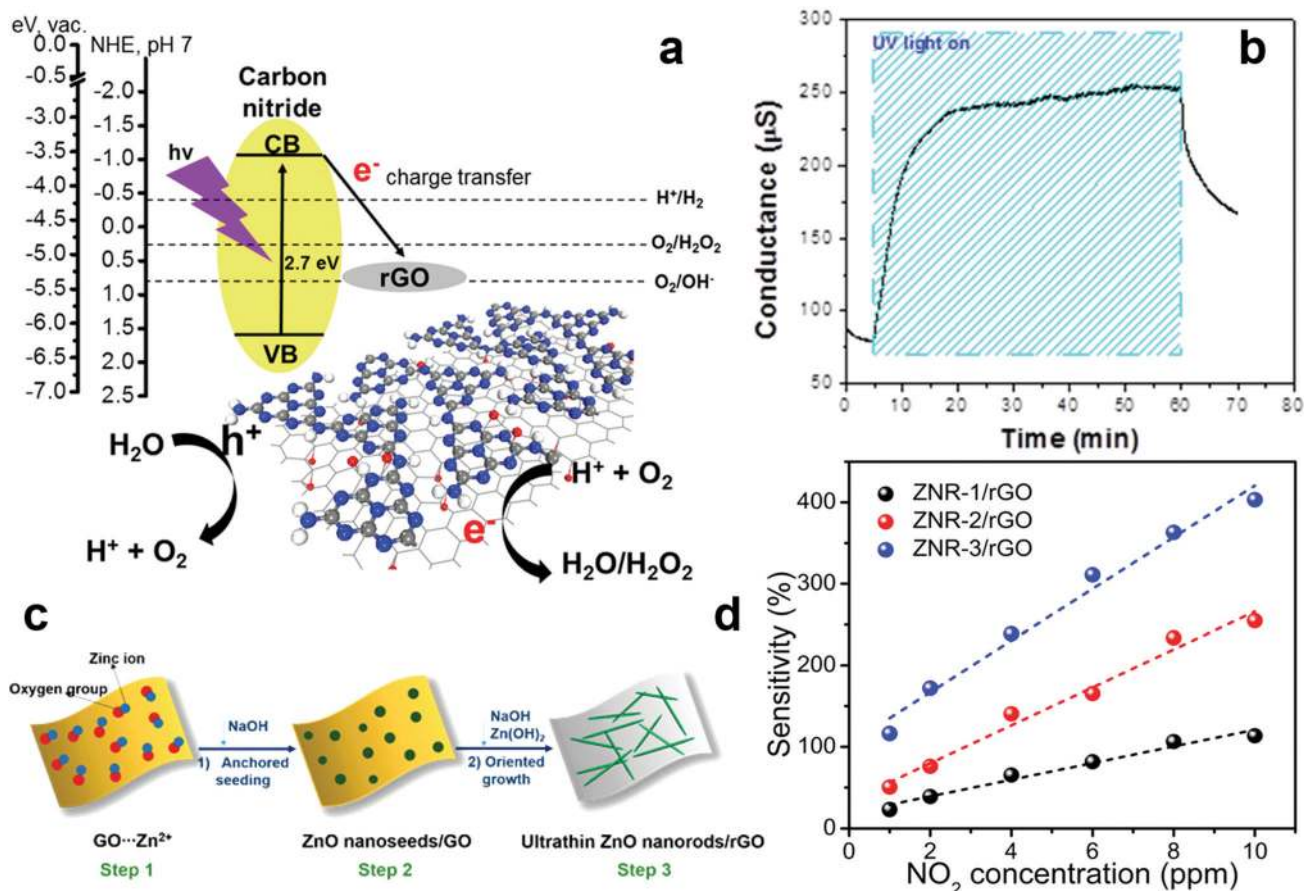
Fig. 1 (a and b) Sensing schematics (a) and conductance (b) of a carbon nitride/RGO oxygen sensor. (c) Schematics for preparation of ZnO nanorod/RGO composites. (d) Sensitivities of ZnO/RGO sensors. Adapted with permission from ref. 74 (a and b) and ref. 77 (c and d). Copyright (2017, 2016) American Chemical Society.

and dioxide,[76] nitrogen dioxide,[77,78] ammonia,[79] water[80] and chemical[81] vapor, hydrogen peroxide,[82] etc.) that directly affect not only the environment, but also industrial safety and specific biomedical fields. Corresponding examples follow below. In order to create an oxygen sensor that is working under UV photo-activation, Ellis et al. have combined polymeric graphitic carbon nitride with RGO by depositing RGO and exfoliated carbon nitride between gold electrodes. The resulting sensor was capable of sensing oxygen in the range of 300–100 000 ppm. This was possible due to a photoredox mechanism that appeared during oxygen reduction on the RGO surface (Fig. 1a).[74] Experiments have further revealed that UV irradiation increased the conductance of the carbon nitride/RGO sensor by 100% (Fig. 1b). This effect was attributed to the charge transfer of excited electrons from carbon nitride to the RGO at the carbon nitride/RGO interface.[74]

Besides oxygen, carbon monoxide can also be detected using RGO based sensors. Such sensors could be fabricated, for example, by doping RGO with nitrogen (NRGO) and by combining NRGO with hierarchical In_2O_3 nanocubes of mesoporous structure. In this way, NRGO–indium oxide nanocube (In_{NRGO}) composites were created. While In_2O_3 nanocubes exhibited good carbon monoxide sensitivity with a LOD of 1 ppm at 250 °C, the In_{NRGO} composites demonstrated a sensitivity up to 3.6 ppm of carbon monoxide,

but at only 35 °C.[75] Instead, carbon dioxide can be detected using a gas sensor made of partially reduced graphite oxide deposited on a $LiNbO_3$ surface acoustic wave (SAW) device. Because SAWs are very sensitive to changes in properties such as mass, dielectric constant and electrical properties at and near the surface, they are ideal platforms for gas sensors. For instance, with such a sensor, 0.43 mg cm^{-3} of carbon dioxide could be detected.[76]

Detection of nitrogen dioxide is possible by designing sensors based on ultrathin ZnO nanorods and RGO sheets. When combined, via a synthetic route that necessitates no additives and that is based on anchored seeding and oriented growth procedures, these two materials formed mesoporous composites (Fig. 1c).[77] Compared to ZnO nanorod sensors and to RGO sensors, ZnO/RGO sensors were shown to exhibit both a faster p-type response and higher sensitivity (an estimated LOD of 50 ppb was reported from sensitivity curves presented in Fig. 1d). This performance was again attributed to the efficient electron transfer taking place through the ZnO/RGO interfaces.[77] Moreover, nitrogen dioxide can also be detected using a low-cost Rayleigh SAW resonator device. For fabrication of such a device, Thomas et al. have arranged two quartz-based Rayleigh SAW resonators in a dual oscillator configuration. While one resonator was acting as the reference, the other resonator was coated with RGO, a good gas-sensitive

candidate exhibiting the ability to monitor changes in surface acoustic properties due to mass loading. The resulting Rayleigh SAW resonator device detected nitrogen dioxide at the ppm level.[78]

Detecting and determining the amount of water molecules in the atmosphere also needs sensitive sensors. RGO can be employed to fabricate humidity sensors that are optically transparent. This was demonstrated by Zaharie-Butucel et al. who have used a convective self-assembly technique to deposit regular arrays of RGO stripes into films/patterns of defined geometry on solid polyethylene terephthalate (PET) substrates. Afterwards, the stripes were connected to a voltage source using two gold electrodes and an RGO sensor with a sensing mechanism based on the dependence of the resistance of the RGO stripes on humidity was obtained.[80] Moreover, the ability of the RGO layers to adsorb moisture could lay the base for realization of sensors based on SAWs when possibly combined with YZ LiNbO$_3$ substrates.[83]

RGO can further be employed in micro-gravimetric sensors (i.e. based on adsorbed mass detection with a resonant micro-cantilever) in order to detect, with a resolution of 5 ppm, vapor of other chemicals such as trimethylamine (TMA).[81] Yu and co-workers have shown that such sensors can be fabricated by growing Au NPs on GO followed by reduction to RGO. The resulting AuNP–RGO could be then functionalized with 11-mercaptoundecanoic acid (11-MUA) and loaded onto a resonant microcantilever sensor. A similar approach for fabrication of another microgravimetric sensor able to detect ammonia was further used by Xia and co-workers[79] who have grown Au NPs on RGO, the latter being previously obtained through thermal expansion of graphite. The Au-NP/RGO sample was then further functionalized with mercaptosuccinic acid (MSA) and loaded onto a resonant microcantilever to be used for micro-gravimetric sensing measurements. These measurements revealed that the fabricated sensor was able to detect ammonia with a LOD < 10 ppm.

Besides gas and various vapor molecules, a variety of other substances, relevant in different branches of biological medicine, as well as in chemical monitoring, need to be detected. For example, thrombin,[84] nimesulide,[85] glucose,[86] dopamine,[87] morin,[88] isorhamnetin[89] or DNA[90] need to be precisely detected for drug, clinical, biomedical and/or pharmacokinetics purposes. Today, this can be done using a variety of novel ultrasensitive RGO based sensors. One such sensor was fabricated by Lan et al. in order to detect thrombin.[84] Initially, they have synthesized 3D-RGO on paper cellulose fiber and then they have used this biocompatible platform possessing high electron-transport ability as a substrate to fabricate a photoelectrochemical device. This device was able to exhibit both specificity and sensitivity towards thrombin with a LOD of about 17 fM. Instead, to detect nimesulide, Govindasamy et al. have drop cast RGO nano-ribbons (RGONR) on a screen-printed carbon electrode (SPCE) that was initially cleaned. The resulting RGONR/SPCE sensors were then able to detect nimesulide in the linear range between 1×10^{-8} and 1.5×10^{-3} M and exhibited a calculated limit of detection (LOD) of 3.5 nM.[85]

For successful detection of glucose, researchers have further exploited the synergistic coupling between the various components of a more complex quaternary composite that was made of hemin, silver coated gold nanostars/nanoparticles (AuNS/NP@Ag) and RGO.[86] Here, AuNSs and AuNPs were prepared using a seed mediated growth method while a kinetically controlled seeded growth strategy was applied. These particles were further used to synthesize AuNS@Ag and AuNP@Ag by addition and reduction of AgNO$_3$. Afterwards, a wet-chemical method based on mixing, ultrasonication and centrifugation of AuNP@Ag/AuNS@Ag and hemin-RGO was utilized to synthesize AuNP@Ag–hemin-RGO and AuNS@Ag–hemin-RGO composites (Fig. 2a). Because the resulting composites were able to oxidize a peroxidase substrate in the presence of H$_2$O$_2$, they have been used to develop a sensitive colorimetric sensor for H$_2$O$_2$. As H$_2$O$_2$ is produced by many oxidative enzymes, including glucose, the H$_2$O$_2$ detection mechanism was further adapted to determine trace amounts of glucose, with a calculated LOD of 425 nM (Fig. 2b).[86] Glucose can be further detected using a fluorescence sensor that is based on phenylboronic acid functionalized RGO (RGO-PBA).[91] Such a sensor uses the concept of the fluorescence quenching property of RGO in response to the diol modified fluorescent probes located in the close vicinity of its surface and is able to detect glucose in the range of 2–75 mg mL^{-1} in aqueous solution.[91]

Dopamine (DA) hormone is an important neurotransmitter that can cause neuronal illnesses in wrong concentrations and therefore it is of paramount importance to detect it in very low concentrations. For that, Oh et al. have developed an organic
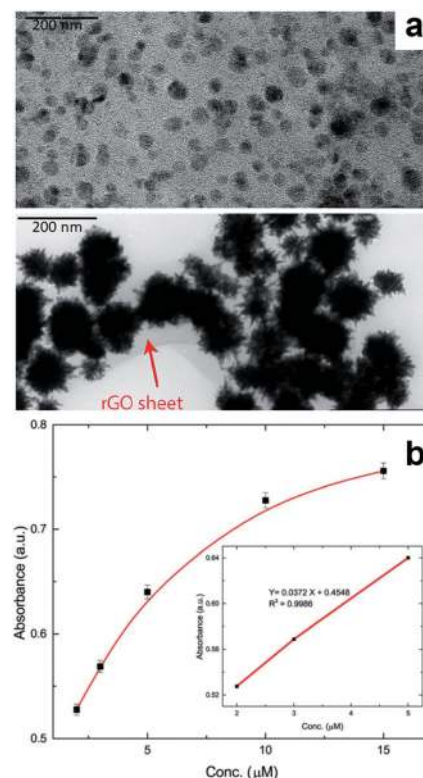

Fig. 2 (a) Transmission electron microscopy (TEM) images of AuNP@Ag–hemin-RGO (top) and AuNS@Ag–hemin-RGO (bottom) composites. (b) AuNS@Ag–hemin-RGO response curve for detection of glucose. Adapted with permission from ref. 86 – published by The Royal Society of Chemistry.

This journal is © The Royal Society of Chemistry 2020

J. Mater. Chem. C, 2020, 8, 1198–1224 | 1201

field-effect transistor-type (FET) sensor without employing an enzyme. They have used platinum nanoparticle-decorated RGO (Pt-RGO) that was made by reducing a GO aqueous dispersion that contained Pt precursors in the presence of a reducing agent. The OFET sensor was then fabricated by immobilization of Pt-RGO on a graphene substrate while a source–drain electrode made from a conducting-polymer was patterned on the same substrate. The resulting sensor, besides being flexible, showed high sensitivity towards DA in concentrations as low as 10^{-16} M.[87] Moreover, when employing FET type sensors, detection in real-time of pathogenic rotavirus could be performed by covalently anchoring specific rotavirus antibodies to the surface of micropatterned RGO.[92] In this case, the LOD for rotavirus was reported to be 10^2 plaque-forming units (pfu). Additional information on other RGO-based FET biosensors can be found in the literature.[93]

Multicomponent composites further lay the base for sensors that can detect antioxidants such as morin. Cheng et al. have fabricated a morin sensor using a glassy carbon electrode (GCE) covered with a poly(3,4-ethylenedioxythiophene)-Au/RGO (PEDOT-Au/RGO/GCE) composite. Fabrication of such an electrode was realized by simply dropping the PEDOT-Au/RGO composite on a polished GCE. PEDOT-Au/RGO/GCE exhibited better performances (a wide linear detection range of 1 to 150 µmol dm^{-3} and a LOD as low as 83×10^{-4} µmol dm^{-3}) towards morin detection when compared to the bare GCE, RGO/GCE and PEDOT-Au/GCE. These performances were attributed to the synergistic effect between the active sites of PEDOT-Au and rather high specific surface area of RGO.[88] A GCE can also be employed to fabricate a rapid yet highly sensitive sensor to detect isorhamnetin (ISO), a dietary flavonoid antioxidant that is found in human plasma and that plays an important role in human health. As it was shown by Peng et al., this is possible by electrochemically reducing RGO covering a GCE. The ERGO/GCE electrode structure detected ISO in rat plasma with a LOD of 3.2×10^{-9} M.[89]

Detection of other biological substances such as trypsin[94] and acetaminophen[95] was recently demonstrated using fluorescence sensors utilizing RGO either alone or functionalized with amphiphilic pillar[5]arene (amPA5). While in the first case RGO was utilized as a fluorescence resonance energy transfer probe acceptor to quench the fluorescent donor emission,[94] in the second case amPA5-RGO is used as a fluorescence sensing platform based on a competitive host–guest interaction between amPA5 and a signal probe comprised of acridine orange and the acetaminophen target molecule (i.e. acetaminophen interacts more strongly with amPA5 than with acridine orange inside the inner cavity of amPA5).[95] Here, a LOD of 0.05 µM for acetaminophen was reported.

Apart from biochemical substances, various other substances related to environmental monitoring are of great interest to be detected, including ions such as Hg^{2+} and Fe^{3+}. As shown by Sudibya and co-workers,[96] RGO-based FET sensors are highly suitable to detect Hg^{2+}. By fabricating a FET sensor using a micropatterned RGO film (functionalized with a protein) as the conducting or sensing channel, the authors were able to detect Hg^{2+} in real-time with a LOD of 1 nM. This performance was further improved a few years later by Park et al., who combined RGO with polyfuran and designed and fabricated a new type of

liquid-ion-gated FET sensor that was capable of detecting Hg^{2+} in heavy metal mixtures with a LOD of 10 pM.[97] Instead, to detect Fe^{3+}, fluorescence sensors based on RGO were recently reported to be efficient.[98] For instance, a polyethyleneimine (PEI)–RGO composite, synthesized using hydrazine hydrate and PEI as reducing agents, could be used to tune the photophysical properties of fluorescein (FL). It was then the FL/PEI–RGO ternary system, which demonstrated a LOD for Fe^{3+} of over 1.1 µM.[98] Other environment related substances such as tricyclazole[99] and thiram[100] pesticides could also be detected using, this time, surface enhanced Raman spectroscopy (SERS) RGO-based sensors. Cat et al. have hydrothermally dispersed crystalline 15 nm sized Ag nanoparticles on the surface of GO sheets in the presence of polyvinylpyrrolidone (PVP), which was used both as a surfactant and reducing agent. The results have indicated that the RGO–Ag composite displayed a high SERS efficiency and sensitivity with the tricyclazole pesticide in the range of 10^{-3}–10^{-6} M, due to the electronic interactions between Ag nanoparticles and graphene.[99] Instead, the thiram pesticide was detected (with a LOD of 5.12×10^{-3} µM) using a SERS sensor based on a hybrid comprised of RGO and Au/Ag core–shell nanorods (RGO–Au@AgNR). Moreover, while the RGO–Ag sensor was also capable of detecting methylene blue (MB) dye in the range of 5×10^{-6} M,[99] the RGO–Au@AgNR sensor could detect Rhodamine 6G (R6G) in the range of 10^{-7} M.[100] Later on, it was demonstrated that R6G could also be detected, in the nM range, using an RGO/Ag NP SERS sensor.[101] Following a similar synthetic route to Cat and co-workers,[99] Naqvi et al. have prepared RGO/Ag NP through decoration of RGO sheets with Ag NPs by reducing $AgNO_3$ with ethylene glycol in the presence of PVP and NaCl over layered GO.[101] Interestingly, besides R6G, the resulting sensor was further capable of detecting, also in the nM range, other substances such as explosives (2,4-dinitro toluene) or organosulfur compounds (4-mercapto benzoic acid).

Wearable sensors are a new category of flexible transparent sensors that recently became very popular in research fields dealing with wearable electronics, electronic skin or robotics. These sensors have been developed using different sensing mechanisms such as impedimetric, potentiometric, capacitance, conductance, piezoelectric, and triboelectric sensing, with their names deriving from the type of resulting signal that is measured. For example, Choi et al. have designed and developed a capacitive touch sensor that is both stretchable and transparent. This sensor displayed touch sensing capabilities based on measuring differences in capacitance for each distance from the touch points.[102] Such a sensor was fabricated by employing a series of spin casting procedures. Firstly, silver nanowires (AgNWs) were spin cast on a polydimethylsiloxane (PDMS) substrate that was pre-treated using oxygen plasma. Secondly, RGO was spin cast on top of the AgNW/PDMS film. Then, a polyurethane (PU) dispersion was spin cast on top of RGO/AgNW/PDMS. At the end, two substrates with the PU surfaces facing each other were pressed at high temperature and pressure followed by the attachment of the contacts.[102]

Detection of human motion was further targeted by Zhao et al. who designed and realized hierarchical architectures that were based on fragmentized RGO sponge (FRGOS) and silver

1202 | J. Mater. Chem. C, 2020, **8**, 1198–1224

This journal is © The Royal Society of Chemistry 2020

nanoparticles (Ag-NP). They have embedded 3D percolation networks of FRGOS in a matrix of poly(styrene-*block*-butadiene-*block*-styrene) (SBS). Then, they have reduced silver ions to Ag-NPs, which were absorbed both inside and on the external surface of the stretchable FRGOS/SBS composites (Fig. 3a).[103] The resulting FRGOS/SBS-Ag-NP architectures, actually inspired by the geometries of animal anatomy (Fig. 3b), have been then used to fabricate highly stretchable yet sensitive (a sensitivity of $\approx 10^7$ at a strain of 120%, Fig. 3c) sensors that were able to detect the modes of finger motions. Here, the sensitivity was attributed to the synergistic effects of the FRGOS architectures and Ag-NPs.[103]

Furthermore, Kim *et al.* have imagined and fabricated multifunctional sensors that could detect human-motion by taking advantage of the bending properties of cotton fabric. For that, commercial cotton fabric was immersed into a GO dispersion, followed by a reduction procedure in hydrazine that led to RGO fabric. The RGO fabric was then hybridized with single-wall carbon nanotubes (SWCNT) by dipping the RGO fabric into SWCNT solutions of various concentrations. This sequence of procedures led to conductive RGO/SWCNT networks.[104] The sensing performance of strain–pressure sensors based on such networks was evaluated by measuring the effects of bending strain and pressure. The results have indicated a clear dependence between the SWCNT content and relative resistance and durability. The obtained sensor exhibited high mechanical stability and

flexibility during a rather large number of bending tests and it was able to successfully detect human motion.[104]

Other bendable sensors, developed on RGO patterned paper substrates, were also shown to be highly sensitive to various deformations and to be capable of measuring very small bending and folding angles.[105] These sensors were fabricated by employing a multilayer masking method that used alternating procedures of cutting and drop-casting. The resulting sensors did not only detect a pulse and the motion of knees, wrists, and fingers, but they could also be used to control a robotic hand.[105]

Being aware that the main characteristics of noncontact electronic skin (*i.e.* flexible, bendable/stretchable electronics that are capable of mimicking functionalities of human skin) are "superior long-range and high-spatial-resolution" sensory properties, An *et al.* have designed and demonstrated a strategy to fabricate all-graphene flexible electronic skins.[106] They have actually exploited a moisture-sensing mechanism that relies on proton and ionic conductivity in different humidity conditions.[106] Using a laser writing method, the authors have designed patterning and reduction of GO thin films, to create a sensor comprised of RGO electrodes and GO sensing layers (see a film containing stacked GO and laser-irradiated porous RGO in Fig. 3d–f). The resulting sensor exhibited selectivity towards moisture and showed good spatial-resolution sensitivity over a rather long detection range in a non-contact mode (Fig. 3g).[106]
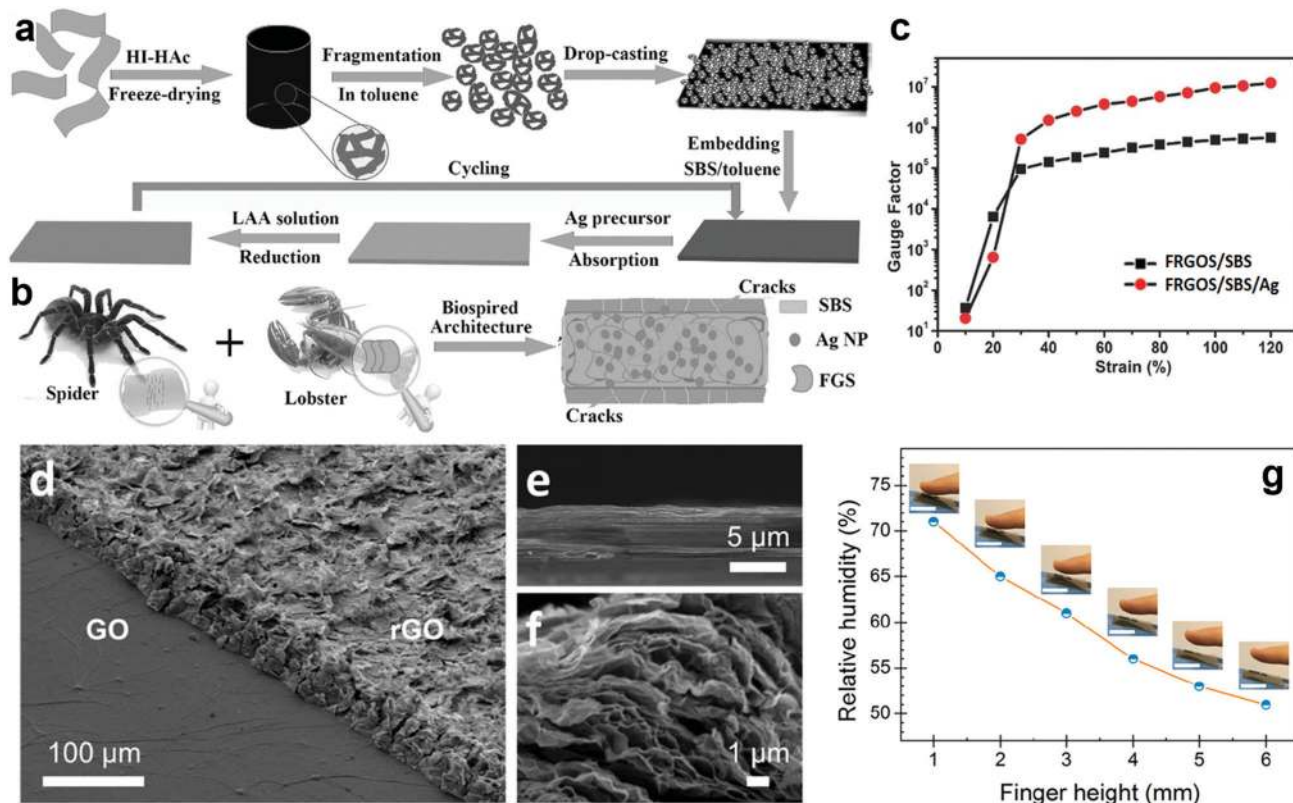

Fig. 3 (a) Schematic fabrication of FRGOS/SBS/Ag composites. (b) Concept of architectures inspired by animal anatomy. (c) Gauge factor *versus* strain measured for both FRGOS/SBS and FRGOS/SBS/Ag composites. (d–f) Tilted (d) and cross-sectional (e and f) scanning electron microscopy (SEM) images of thin films of stacked GO and porous RGO. (g) Variation in the calibrated relative humidity of a fingertip with sensing distance (the scale bar is 20 mm). Adapted with permission from ref. 103 (a–c) and ref. 106 (d–g). Copyright (2012) John Wiley and Sons Ltd and (2017) American Chemical Society.

This journal is © The Royal Society of Chemistry 2020

J. Mater. Chem. C, 2020, **8**, 1198–1224 | **1203**

In summary, it is hard to imagine a future without continuous development of novel, better performing sensors. For that, novel materials and composites need to be continuously designed and developed. An example of such materials could possibly be $WO_3 \cdot 0.33H_2O$ nano-needles[107] or flexible and stretchable RGO-based fibers containing, for example, semiconducting CuI and metallic Cu particles. Although difficult to synthesize, such fibers could be suitable for the next-generation of wearable multi-sensors and electronics.[108] Our most important findings related to RGO-based sensors are summarized in Table 1. Additional information on such sensors can further be consulted in the literature.[109]

RGO – a key component in electrode structures used in various battery technologies

In the present day, there is high demand for energy storage systems that need to power a tremendous diversity of continuously increasing portable and wearable electronic devices, including personal computers, watches, smartphones, more and more electric vehicles, *etc.* The most efficient technology used to power such electronic devices is represented by batteries, *i.e.* devices that consist of one or more electrochemical cells that are able to convert chemical energy into electrical energy. There are several technologies to realize efficient batteries, but the technology of lithium-ion batteries (LIBs) is the most reliable, mostly due to the long cycle life, high energy density, high working voltage, *etc.* Compared to conventional heavy/rigid LIBs, novel LIB systems are required to be lightweight, flexible, miniaturized, high capacity, eventually low cost, reliable and safe, *etc.* Therefore, new structures and novel materials are continuously designed and developed in order to realize advanced electrodes for LIBs that could satisfy the above-mentioned demands. RGO is light, flexible and possesses an electrical conductivity that can reach even $97\,500$ S m^{-1} in few micrometre thick films.[112,113] Therefore, it could potentially increase the conductivity of various composites, it could improve the electrode performance and it could lead to diminished battery volume and weight. Recent examples of advanced RGO-based electrodes for LIBs are further exemplified below.

Table 1 Characteristics of RGO-based sensors

Type of sensor	Sensitive material	Substance/deformation detected	LOD	Ref.
Electrochemical	PEDOT-Au/RGO/GCE	Morin	83×10^{-4} µmol dm^{-3}	88
Electrochemical	N-Doped RGO/In$_2$O$_3$	Carbon monoxide	3.6 ppm	75
Electrochemical	Carbon nitride/RGO	Oxygen	300–100k ppm	74
Electrochemical	ZnO NR/RGO	Nitrogen dioxide	50 ppb	77
Electrochemical	ERGO/GCE	Isorhamnetin	3.2×10^{-9} M	89
Electrochemical	Cu-TDPAT-n-ERGO	Hydrogen peroxide	0.17 µM	82
Electrochemical	3D-RGO/cellulose fiber/DNA	Thrombin	16.7 fM	84
Electrochemical	AuNP/S@Ag–hemin-RGO	Glucose	1.26 nM	86
		Hydrogen peroxide	425 nM	
Electrochemical	RGONR/SPCE	Nimesulide	3.5 nM	85
FET	Pt–RGO on graphene	Dopamine	10^{-16} M	87
FET	Micropatterned RGO	Rotavirus	10^2 pfu	92
FET	Micropatterned RGO	Hg^{2+}	1 nM	96
		Ca^{2+}	1 µM	
		Mg^{2+}	—	
FET	RGO–polyfuran hybrid	Hg^{2+}	10 pM	97
FET	RGO/ferritin	Orthophosphate ions	26 nM	110
SERS	RGO–Au@AgNR	Thiram	5.12×10^{-3} µM	100
		Rhodamine 6G	10^{-7} M	
SERS	RGO–Ag	Tricyclazole	10^{-3}–10^{-6} M	99
		Methylene blue	5×10^{-6} M	
SERS	Ag nanocube–RGO	Thiram	44 nM	111
		Ferbam	38 nM	
SERS	AgNP@RGO	DNA	10^{-6} M	90
SERS	RGO/Ag NP	Rhodamine 6G	nM level	101
		2,4-Dinitrotoluene		
		4-Mercaptobenzoic acid		
Fluorescence	amPA5–RGO	Acetaminophen	0.05 µM	95
Fluorescence	RGO–PBA	Glucose	2–75 mg mL^{-1}	91
Fluorescence	RGO	Trypsin	—	94
Fluorescence	FL/PEI–RGO Fe^{3+}	Fe^{3+}	1.1 µM	98
Gravimetric	AuNP–RGO/11-MUA	Trimethylamine	5 ppm	81
Gravimetric	Au-NP/RGO/MSA	Ammonia	<10 ppm	79
Acoustic	Quartz Rayleigh resonators/RGO	Nitrogen dioxide	ppm level	78
Acoustic	Partially RGO/YZ LiNbO$_3$	Water molecules/humidity	—	83
Mechanical	PU/RGO/AgNW/PDMS	Touch sensing	—	102
Mechanical	RGO-paper	Bending angle	0.2°	105
		Folding angle	0.1°	
Mechanical	RGO/SWCNT networks	Bending strain	11.6%	104
Mechanical	RGO stripes on PET	Strain	1%	80
		Humidity	10% RH	
Electronic skin	GO/RGO	Water molecules/humidity	—	106

This journal is © The Royal Society of Chemistry 2020

The most widely used material in fabrication of LIBs is titanium oxide, and our first example is a novel fiber battery electrode based on this material. Here, titanium oxide was firstly processed into 2D nanosheets and then assembled into a macroscopic fiber using mixing along with a wet-spinning approach (Fig. 4a).[114] Such nanosheets were regularly stacked and then further hybridized *in situ* with RGO. This process led to a fiber electrode that exhibited both improved mechanical flexibility and good battery performances in terms of cyclic behavior and rate capability. For example, the titanium/RGO fiber electrode could retain a specific capacity of almost 90 mA h g^{-1} (Fig. 4b).[114]

Improvement of LIB performances was further targeted by increasing the dimensionality of the material to 3D conductive structures. Meng *et al.* have used an ammonium chloride agent to prepare 3D "fishnet-like" lithium titanate (LTO)/RGO composites with hierarchical porous structure. This was done by employing a gas-foaming method that was able to disperse tens of nanometers sized LTO particles on the 3D "fishnet-like" RGO.[115] The resulting porous nature of the LRO/RGO structure has facilitated better penetration of electrolytes and it actually improved the diffusion of lithium ions. Therefore, the specific capacity exceeded a value of 176 mA h g^{-1} at a rate of 1C. The LRO/RGO electrodes exhibited excellent cycle performance (with over 95% capacity retention at 10 C after 100 cycles) and demonstrated this composite as a highly promising anode material for LIBs.[115]

Good performances for advanced lithium storage based on the improvement of electrolyte ion diffusion in the electrode were further reported by Ma *et al.* for another 3D porous hybrid. This hybrid was made of RGO and MXenes (*i.e.* 2D materials exfoliated from ternary carbide and nitride ceramics possessing both metallic conductivity and a hydrophilic surface with rich chemistry).[116] They have imprinted a 3D porous structure in MXene/RGO hybrid films using self-assembly. The resulting porous film electrode has demonstrated a high specific capacity (over 335 mA h g^{-1} at 0.05 A g^{-1}), good rate capability (30% capacitance retention at 4 A g^{-1}) and cycling stability with no capacity decay even after 1000 cycles.[116]

3D porous structures were further used by Xiao *et al.* as a replacement for metal-foil current collectors in LIBs.[117] More precisely, they have synthesized from graphite and poly(acrylic acid) (PAA) a highly porous 3D RGO/PAA composite aerogel that could be compressed 30-fold without mechanical damage and it could increase the ion transport rate. When compared to Al foil, the RGO/PAA electrode displayed an increased effective area (*i.e.* an increased volumetric capacity) without compromising the electrode density.[117]

Recently, several other binary and even ternary composites of porous nature and possessing superior performances as anodes in LIBs were reported in the literature.[118–120] For instance, Qi *et al.* have pulverized small FeOOH rods on RGO sheets and have created a porous composite electrode that was capable of achieving high energy density and good cycling performance for more than 200 cycles at different current densities (*i.e.* 1135 mA h g^{-1} at 1 A g^{-1}, Fig. 4c).[118] Good performances, including increased electrical conductivity ($\sim 10^{-3}$ S cm^{-1}) and high charge capacity (over 1165 mA h g^{-1} at 100 mA g^{-1}, Fig. 4d), were also reported for a SnC$_2$O$_4$/RGO composite (Fig. 4e, bottom left). This composite was produced by combining hydrothermal reactions with layer-by-layer self-assembly (Fig. 4e) and it was able to deliver 620 mA h g^{-1} at the 200th cycle.[119] Besides these binary composites, Shah *et al.*
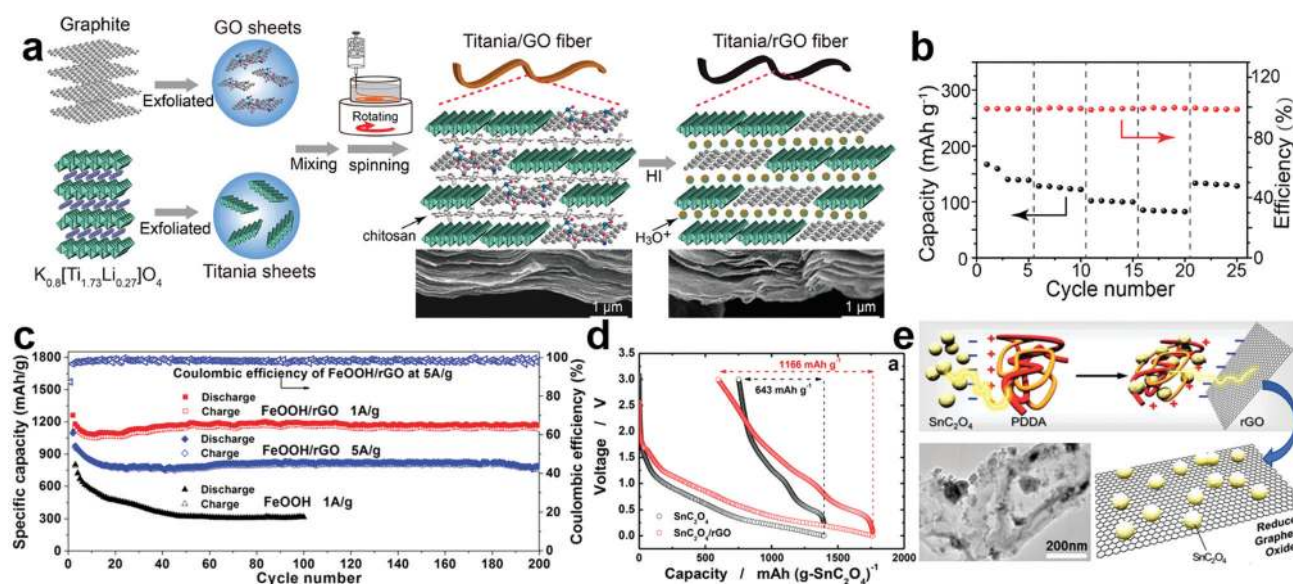

Fig. 4 (a) Schematics of titania/GO and titania/RGO fiber fabrication (left) along with SEM images of dry titania/GO and titania/RGO fibers reduced in hydroiodic acid (right). (b) Rate capabilities corresponding to titania/RGO fiber electrodes at different current densities. (c) Cycling capability of FeOOH and FeOOH/RGO composites. (d) First discharge and charge plots measured for SnC$_2$O$_4$/RGO. (e) Schematics of SnC$_2$O$_4$/RGO synthesis along with the TEM image of SnC$_2$O$_4$/RGO. Adapted with permission from ref. 114 (a and b), ref. 118 (c) and ref. 119 (d and e). Copyright (2017, 2016) American Chemical Society.

This journal is © The Royal Society of Chemistry 2020

J. Mater. Chem. C, 2020, 8, 1198–1224 | 1205

have synthesized, using a hydrothermal method, highly inter-digitated and yet porous ternary composites comprised of 2D SnS$_2$, RGO and graphitic carbon nitride (g-C$_3$N$_4$). The results have shown that composite anodes that contained several weight% g-C$_3$N$_4$ exhibited the best specific capacity ($\sim$1250 mA h g^{-1} after more than 275 cycles with a coulombic efficiency of almost 100% at 100 mA g^{-1}). These performances were attributed to the unique 3D porous structure, which facilitated both charge transfer and lithium ion diffusion.[120]

Porous CuO nanospheres[121] and Fe$_3$S$_4$ nanoparticles[122] were further decorated on RGO, *via* thermal treatment procedures, to create porous CuO/RGO and Fe$_3$S$_4$/RGO composites for enhancement of lithium anodes. Studies suggested that the porosity of the CuO/RGO composite improved the lithium storage performances, including the reversible capacity (over 753 mA h g^{-1} at 100 mA g^{-1}) and cycling stability (over 616 mA h g^{-1} after 200 cycles at 500 mA g^{-1}).[121] Instead, Fe$_3$S$_4$ nanoparticles sandwiched with RGO led to Fe$_3$S$_4$/RGO anode composites with increased cycling capacity due to neglectable aggregation of intermediate phases during the discharge/charge process. Moreover, the interconnected RGO sheets acted as a highly conductive network that enhanced the electrochemical reactions and finally facilitated the lithiation/delithiation of Fe$_3$S$_4$ nanoparticles.

Therefore, the resulting Fe$_3$S$_4$/RGO anode was shown to be capable of a reversible charge capacity of more than 1320 mA h g^{-1} over 275 cycles.[122]

It is worth mentioning that besides LIBs there is growing interest in realizing other types of RGO based batteries such as sodium ion batteries (SIBs),[123,125–127] lithium–sulfur batteries (LiSBs)[124] or aluminum batteries.[128] Li *et al.* have suggested that SIBs are feasible when they have fabricated a Fe$_2$O$_3$/RGO composite anode (shown in Fig. 5a, right) by anchoring Fe$_2$O$_3$ single crystallites (Fig. 5a, left) on RGO nanosheets. This process led to a highly conductive and yet flexible structure, with good electron transport. As a consequence, the Fe$_2$O$_3$/RGO composite anode showed an initial discharge/charge capacity of over 860 mA h g^{-1} (Fig. 5b), a good coulombic efficiency (over 70% at the first cycle) and cyclability (with about 82% capacity retention after 100 cycles).[123] A specific capacity reaching 1230 mA h g^{-1} and a rate capability of 445 mA h g^{-1} at 5000 mA g^{-1} were further reported for anode materials that were obtained from mixed Sn–S ultrafine nanoparticles distributed on RGO by combining hydrothermal synthesis with carbothermal reduction.[126]

Besides anchoring crystallites or distributing mixed nanoparticles on RGO, researchers have reported the possibility to dope RGO with iodine in order to fabricate an anode material
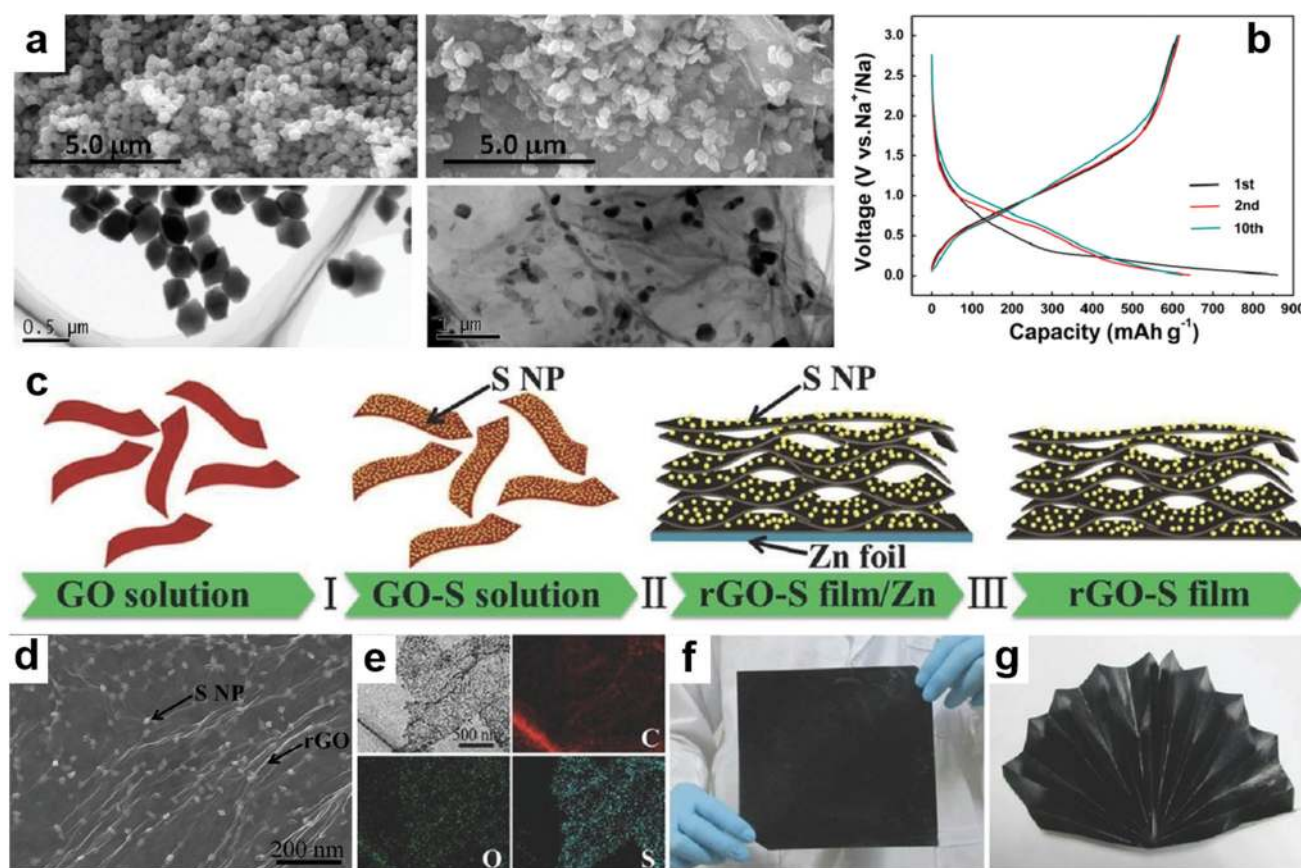

Fig. 5 (a) SEM and TEM micrographs of Fe$_2$O$_3$ (left) and the Fe$_2$O$_3$/RGO composite (right). (b) Charge/discharge plots recorded for the Fe$_2$O$_3$/RGO electrode. (c) Schematics of fabricating RGO−S composite films. (d) SEM image depicting an RGO−S film. (e) TEM elemental mapping of carbon, oxygen, and sulphur on top of an RGO sheet. (f and g) Optical images of an RGO−S composite film before and after folding. Adapted with permission from ref. 123 (a and b) and ref. 124 (c and h). Copyright (2017) American Chemical Society and (2016) John Wiley and Sons Ltd.

1206 | *J. Mater. Chem. C*, 2020, **8**, 1198–1224

This journal is © The Royal Society of Chemistry 2020

Table 2 Characteristics of RGO-based batteries

Battery	Material	Synthesis method	Retention/cycling capacity	Capacity	Ref.
LIB	Titania/RGO	Spinning/hybridization	70% (200 cycles@8.5 µA)	89 mA h g^{-1}@42.5 µA	114
LIB	LTO/RGO	Gas-foaming dispersion	95.4% (100 cycles@10C)	176.6 mA h g^{-1}@1C	115
LIB	MXene/RGO	Induced self-assembly	100% (1000 cycles@1 A g^{-1})	335.5 mA h g^{-1}@0.05 A g^{-1}	116
LIB	3D RGO/PAA	Thermal annealing	83% (200 cycles@0.2C)	146 mA h g^{-1}@0.2C	117
LIB	FeOOH/RGO	Pulverisation	83.9% (200 cycles@5 A g^{-1})	1443 mA h g^{-1}@0.2 A g^{-1}	118
LIB	SnC$_2$O$_4$/RGO	Hydrothermal/self-assembly	53% (200 cycles@0.1C)	1166 mA h g^{-1}@0.1C	119
LIB	SnS$_2$/RGO/g-C$_3$N$_4$	Hydrothermal reduction	1248.4 mA h g^{-1} (276 cycles@100 mA g^{-1})	—	120
LIB	CuO NS/RGO	Thermal reduction	616.2 mA h g^{-1} (200 cycles@0.5 A g^{-1})	753.3 mA h g^{-1}@100 mA g^{-1}	121
LIB	Fe$_3$S$_4$/RGO	Thermal reduction	480 mA h g^{-1} (500 cycles at 1 A g^{-1})	1324 mA h g^{-1}@100 mA g^{-1}	122
LIB	Fe$_2$O$_3$/RGO	Solvothermal anchoring	82% (100 cycles@50 mA g^{-1})	610 mA h g^{-1}@50 mA g^{-1}	123
SIB	Iodine/RGO	Doping	212 mA h g^{-1} (100 cycles@50 mA g^{-1})	270 mA h g^{-1}@50 mA g^{-1}	127
SIB	Sn–S NP/RGO	Hydro- and carbothermal reduction	91% (50 cycles@50 mA g^{-1})	1230 mA h g^{-1}@25 mA g^{-1}	126
SIB	Holey RGO	H$_2$O$_2$ treatment and reduction	163 mA h g^{-1} (3000 cycles@2 A g^{-1})	365 mA h g^{-1}@0.1 A g^{-1}	125
LiSB	RGO–S NP	Reduction and structuring	75% (200 cycles@0.1C)	1302 mA h g^{-1}@0.1C	124
AlB	RGO powder	Thermal reduction	85% (100 cycles@100 mA g^{-1})	171 mA h g^{-1}@100 mA g^{-1}	128

for SIBs. The doping process was used to increase the spacing between the RGO sheets and to introduce positive charge density to the surface of RGO, leading to an iodine/RGO anode. Compared to bare RGO, this anode facilitated sodium ion storage and improved the electron transport and sodium ion diffusion. Therefore, the iodine/RGO anode reached a reversible capacity of 270 mA h g^{-1} at 50 mA g^{-1} and a cycling capacity of over 210 mA h g^{-1} after 100 cycles.[127] Moreover, new hybrids obtained through reduction of GO with the emphasis on encapsulation of CuP$_2$ nanoparticles into 3D graphene networks recently launched novel concepts in SIBs.[129] The fabricated electrodes could deliver a reversible capacity of over 800 mA h g^{-1} at 0.1 A g^{-1}.

Yet another example indicates that LiSBs can be fabricated using components such as flexible RGO–S composite films that can be obtained by reducing and structuring GO sheets with S nanoparticles (Fig. 5c). Through this process, S nanoparticles usually end up homogeneously distributed on a metal surface, as it is emphasized in the SEM image in Fig. 5d and by the TEM mapping in Fig. 5e. Because of their nanostructured nature, RGO–S composite paper-like films possess multiple capabilities. They can bend and fold without cracking (Fig. 5f and g), can facilitate electron transport, and can suppress the diffusion of polysulfides, and thus can deliver great electrochemical performances.[124] All these capabilities make RGO–S composites an ideal candidate for realization of flexible LiSBs. Finally, our most important findings related to RGO-based sensors are summarized in Table 2.

Employing RGO to fabricate hybrid structures for supercapacitors

Supercapacitors are electric capacitors that are used in various electronic devices for energy storage. They display a long cycle life and possess various functions including the ability to store a high amount of energy (for example, per unit volume), to exhibit high capacitance or to charge and discharge at high rates. There are three categories of supercapacitors: electrochemical double layer capacitors (EDLCs), pseudocapacitors (PCs) or redox supercapacitors and hybrid capacitors (HCs), depending on their

energy storage mechanisms. EDLCs store high charge at the electrode–electrolyte interface with their capacitance arising from the separated electric charges at this interface. The advantage of EDLCs consists in their capability to deliver high power density, but at the cost of low energy density and limited rate capability.[130] Instead, in PCs the capacitance is from an electrochemically reversible rapid faradaic reaction that is produced at the electrode–electrolyte interface. The advantage of PCs consists in their capability to display high energy density, but accompanied by low power density and absent cyclic stability.[131] There are various carbon-based materials that are used to fabricate EDLCs and they include activated carbon, CNTs, carbon fibers or graphene. Pseudocapacitive materials used for fabrication of PCs are generally metal oxides and hydroxides, metal nitrides, metal carbides or conducting polymers.[132,133] Hybrid materials combining carbon-based materials and pseudocapacitive materials can be exploited in order to design and develop HCs that combine the advantages of both EDLCs and PCs and thus display high energy storage, high power density and longer cycle stability. RGO has been used in each of these types of supercapacitors,[134–136] while currently many new material configurations and techniques are being investigated.[137–139] Examples of RGO-based EDLCs and HCs follow below.

To fabricate an efficient EDLC, Bhattacharya et al. have coated iron oxide (Fe$_3$O$_4$) nanoparticles with π-conjugated 2-aminoterephthalic acid (ATA). Then, using a combination of wet chemistry and sonication, they mixed them with RGO and obtained the ATA-Fe$_3$O$_4$/RGO composite. This composite exhibited a specific capacitance of over 575 F g^{-1} (see Fig. 6a).[140] This value was significantly higher than the value obtained for the pristine Fe$_3$O$_4$ and RGO components. Here, the role of the ATA coating of Fe$_3$O$_4$ nanoparticles was not only to improve the charge transfer process of Fe$_3$O$_4$, but also to utilize various functional groups located on RGO to enhance the capacitance.[140] RGO further proved itself to be a useful material in fabrication of asymmetric EDLCs.[141] By growing photovoltaic quaternary chalcogenide Cu$_2$NiSnS$_4$ (QC) nanoparticles on 2D RGO, Sarkar et al. have obtained a composite that could be used to fabricate anodes for asymmetric supercapacitors. Such anodes were capable of delivering an areal capacitance of over 655 mF cm^{-2} (as calculated from the

This journal is © The Royal Society of Chemistry 2020

J. Mater. Chem. C, 2020, 8, 1198–1224 | 1207

gravimetric capacitance of 164 F g^{-1}) and a volumetric capacitance of over 16 F cm^{-3} (see Fig. 6b).[141] Interestingly, the areal capacitance value reported for this composite exceeded the value of commercial supercapacitors.[141]

Aqueous[142] and gel-electrolyte[134] EDLCs can also be fabricated by employing RGO and carbon nanotubes (CNT). Aqueous supercapacitors involve cathodes comprised of manganese molybdate (MnMoO$_4$) sheets. Such sheets can be grown hydrothermally, with or without RGO, on 3D nickel supported CNT substrates.[142] Because of the synergistic effects occurring between each composite component, the CNT/RGO/MnMoO$_4$ cathodes were shown to be capable of exhibiting a specific capacitance of almost 2375 F g^{-1} (at a scan rate of 2 mV s^{-1}) and maintaining over 97% of the initial specific capacitance even after 3000 charge/discharge cycles.[142] Instead, using the same scan rate, a more modest specific capacitance (over 93 F g^{-1}) could be measured for CNT–RGO/H$_2$SO$_4$–polyvinyl alcohol (PVA) gel-electrolyte supercapacitor electrodes. These electrodes could be fabricated by applying screen printed pastes of RGO and CNTs on carbon cloth to the H$_2$SO$_4$–PVA electrodes.[134]

Furthermore, it is worth mentioning that, today, a more and more desirable property of EDLCs is their flexibility. Flexible RGO-based EDLCs could be fabricated by using free-standing flexible composite films made of activated carbon and RGO (AC/RGO).[143] AC/RGO film-like electrodes were made by heating a mixture of AC and GO in the presence of hydrazine hydrate followed by filtration through a membrane.[143] At the

optimal ratio of AC and RGO (*i.e.* 2 : 1) these flexible and yet lightweight film electrodes have exhibited a specific capacitance of $\sim$200 F g^{-1}. Moreover, they have retained 85% and 95% of their capacitance even after 10 000 charging/discharging and 1000 bending cycles, respectively.[143]

As in the case of EDLCs, there are many studies demonstrating the superior efficiency of PCs made of various pseudocapacitive materials[132] and RGO. Here, we will mention only a few reports of RGO-based pseudocapacitive composites. One such report was published by Chang *et al.* who prepared the RGO/Ni(OH)$_2$ pseudocapacitance composite by combining the reduction of GO using polyvinylpyrrolidone with the subsequent hydrolysis of Ni(Ac)$_2$ on RGO.[144] Due to synergetic effects, RGO/Ni(OH)$_2$ exhibited better capacitance and rate performance than did the pure Ni(OH)$_2$, with the specific capacitance remaining at 840 F g^{-1} after a rather modest number of 1000 charge and discharge cycles.[144] Instead, significantly longer cyclability of PCs (over 10 000 cycles) was reported by Bhattacharya *et al.* who integrated CoO nanoparticles with ozonized RGO using ice templating and thermal annealing. In this way, they have obtained a CoO/RGO composite that was not only capable of rapidly transporting ions, but also of exhibiting low charge transfer resistance. These properties of the CoO/RGO composite were responsible for the reported fast/reversible pseudocapacitance.[145] Moreover, when utilizing a Cu$_2$O/CuO/RGO composite synthesized through a hydrothermal-assisted redox reaction starting from a nanoporous Cu source and GO, even a much longer cyclability of PCs can be obtained.
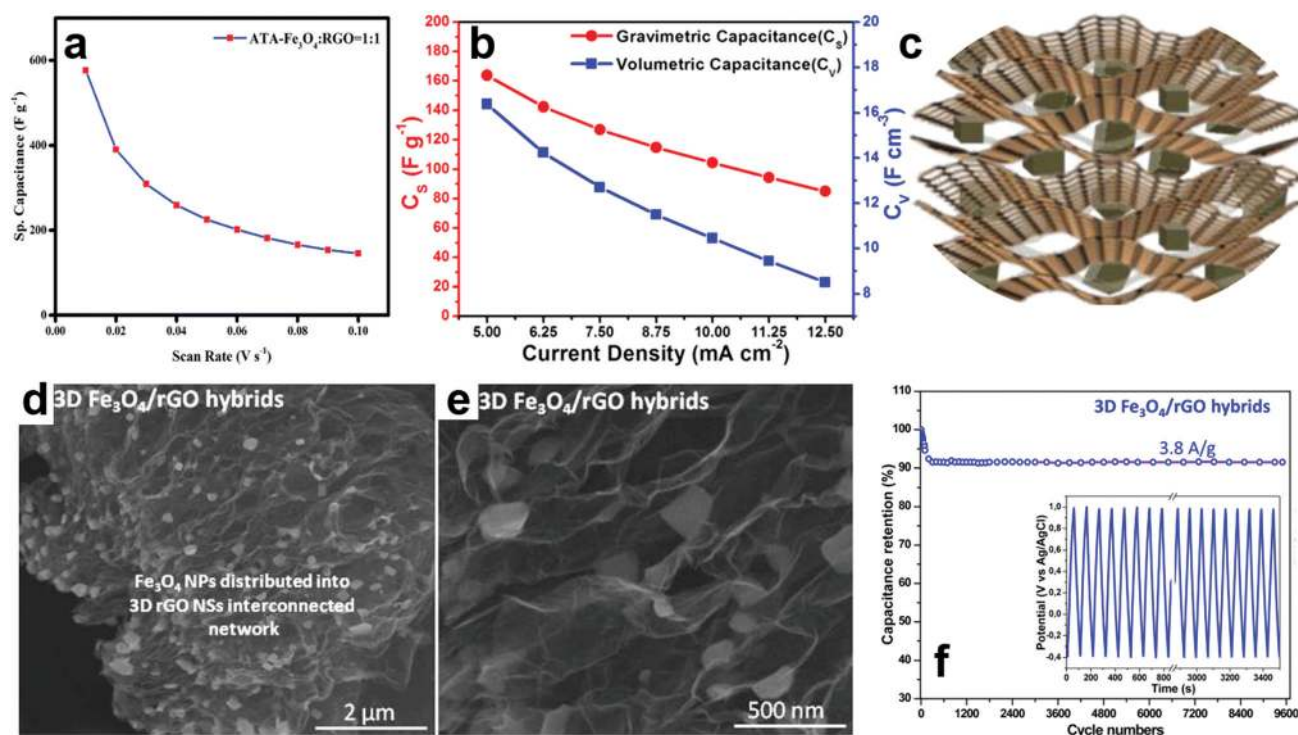

Fig. 6 (a) Specific capacitance *vs.* scan rate recorded for the ATA-Fe$_3$O$_4$/RGO composite. (b) Calculated gravimetric and volumetric capacitances of an asymmetric supercapacitor at different current densities. (c) Schematic representation of the 3D Fe$_3$O$_4$/RGO hybrid. (d and e) SEM images of the 3D Fe$_3$O$_4$/RGO hybrid at magnifications of 2 μm (d) and 500 nm (e), respectively. (f) Cycling stability of the Fe$_3$O$_4$/RGO electrode (inset: time *vs.* potential in charge/discharge). Adapted with permission from ref. 140 (a), ref. 141 (b) and ref. 136 (c–f). Copyright (2017) American Chemical Society. Ref. 140 – published by The Royal Society of Chemistry.

Wang *et al.* have demonstrated that the capacity can stay rather unchanged (over 98%) even after 100 000 cycles.[146] Other interesting work related to RGO-based PCs can be further consulted in the literature.[147,148]

In order to fabricate HCs, Kumar *et al.* have embedded Fe_3O_4 nanoparticles in 3D RGO sheets (schematically depicted in Fig. 6c) made of graphite oxide powder by combining self-assembly with a microwave-based method. As revealed by SEM measurements (Fig. 6d and e) and various spectroscopies, the internal structure of the Fe_3O_4/RGO hybrid was comprised of faceted Fe_3O_4 nanoparticles introduced between interconnected RGO sheets.[136] Electrochemical studies conducted on an electrode coated with Fe_3O_4/RGO have revealed a cycling stability up to 9600 cycles (see the characteristic charge/discharge curve in Fig. 6f) and a specific capacitance of 455 F g^{-1}. This value was superior to that obtained, for instance, for bare Fe_3O_4 nanoparticles.[136]

Another interesting example of a hybrid material for HCs is that of copper/RGO/manganese dioxide (Cu/RGO/MnO_2) fiber electrodes. Huang *et al.* followed a rather complex preparation procedure to prepare Cu/RGO/MnO_2 fiber electrodes. Here, a glass pipeline that contained a Cu wire and GO suspension was heated at high temperature. The resulting Cu/RGO fiber was refluxed in $KMnO_4$ solution. Finally, flexible fiber supercapacitors were realized by aligning two Cu/RGO/MnO_2 fiber electrodes in a parallel configuration in the presence of a gel electrolyte.[135] The obtained supercapacitors have displayed an areal specific capacitance of 140 mF cm^{-2}. In this case, retentions of capacitance of 88% and 97%, corresponding to more modest numbers of charging/discharging (5000) and bending cycles (500), were measured.[135]

Ruthenium nanoparticles were further used to design and fabricate a Ru_{nano}-based RGO hybrid for HCs as it was shown by Hassan and co-workers.[149] By controlling specific synthesis parameters such as pH, the structure of this hybrid material could be optimized to display good supercapacitor performance in a neutral electrolyte. For example, the Ru_{nano}-based RGO hybrid that was synthesized at pH 8 demonstrated a specific capacitance of 270 F g^{-1} along with good cycling stability.[149] The performance of HCs can be further enhanced by enhancing the packing density in supercapacitors and thus reaching higher volumetric energy density. This can be done by controlling the restacking of RGO sheets through the synthesis of doped scroll structures.[150] Practically, Fe_2O_3 nanoparticles can be encapsulated in RGO scrolls through a synthesis procedure based inclusively on dispersion, sonication and annealing of a GO/Fe_2O_3 mixture in water. A supercapacitor made of Fe_2O_3 doped RGO scrolls is then able to exhibit a volumetric energy density of almost 50 W h L^{-1}.[150] The most important findings related to RGO-based supercapacitors are summarized in Table 3.

Role of RGO in optoelectronic devices and absorption-based applications

Today, there is growing interest in flexible and stretchable devices in all emerging technologies, including optoelectronics. Thin transparent conductive films represent the foundation of

Table 3 Characteristics of RGO-based supercapacitors

Superc.	Material	Synthesis method	Energy density	Retention/cycling capacitance	Capacitance	Ref.
EDLC	ATA-Fe_3O_4/RGO	Wet chemistry and sonication	75 W h kg^{-1}	86% (5000 cycles@6 A g^{-1})	576 F g^{-1} @10 mV s^{-1}	140
EDLC	Cu_2NiSnS_4/RGO	Hydrothermal reduction	5.68 mW h cm^{-3}	89.2% (2000 cycles@5 mA cm^{-2})	655.1 mF cm^{-2}@5 mA cm^{-2}	141
EDLC	CNT/RGO/$MnMoO_4$	Hydrothermal growth	59.4 W h kg^{-1}	97.1% (3000 cycles@2 mV s^{-1})	2374 F g^{-1}@2 mV s^{-1}	142
EDLC	CNT–RGO/H_2SO_4–PVA	Screen printing	—	97.46% (1000 cycles@200 mV s^{-1})	93.1 F g^{-1}@2 mV s^{-1}	134
EDLC	AC/RGO	Thermal reduction and filtration	16.2 μW h cm^{-2}	85% (10000 cycles@5 mA cm^{-2})	486 mF cm^{-2}@0.2 mA cm^{-2}	143
PC	RGO/Ni(OH)$_2$	Reduction and hydrolysis	63.5 W h kg^{-1}	840 F g^{-1} (1000 cycles@6 A g^{-1})	1828 F g^{-1}@1 A g^{-1}	144
PC	Cu_2O/CuO/RGO	Redox reaction	—	98.2% (100000 cycles@10 A g^{-1})	173.4 F g^{-1}@1 A g^{-1}	146
PC	3D CoO/RGO	Thermal annealing and templating	1.086 W h L^{-1}	93.2% (10000 cycles@10 A g^{-1})	239.4 F g^{-1}@10 A g^{-1}	145
PC	RGO paper/Ni–Mn LDH/graphene	Filtration process	—	95% (10000 cycles@4 mA cm^{-2})	217.8 mF cm^{-2}@2 mA cm^{-2}	148
HC	Fe_3O_4/RGO	Microwave heating	124 W h kg^{-1}	91.4% (9600 cycles@3.8 A g^{-1})	455 F g^{-1}@8 mV s^{-1}	136
HC	Cu/RGO/MnO_2	Thermal annealing	—	88% (5000 cycles@20 mV s^{-1})	140 mF cm^{-2}@0.1 mA cm^{-2}	135
HC	Ru_{nano}–RGO	Chemical reduction	15.0 W h kg^{-1}	92.5% (5000 cycles@5 mV s^{-1})	270 F g^{-1}@5 mV s^{-1}	149
HC	Fe_2O_3 doped RGO	Dispersion, sonication and thermal annealing	49.66 W h L^{-1}	88% (10000 cycles@2.4 A g^{-1})	168 F g^{-1}@0.26 A g^{-1}	150

optoelectronics and RGO films could find too their place in such applications. For example, silver-decorated RGO (Ag-RGO) hybrid sheets could be used as building blocks to fabricate transparent flexible films that are much more conductive.[151] With fine tuning of the silver content, Ag-RGO films achieved a sheet resistance two orders of magnitude lower than that of RGO films.[151] A greater conductivity was also reported for RGO–WO_3 composites, compared to that of the WO_3 nanorods only.[152] Here, RGO has enhanced the dielectric modulus and the interfacial polarization.[152] Other RGO properties such as the optical bandgap can also be altered.[153] Thus, RGO can be regarded as a highly appealing material for optoelectronic applications. To strengthen this statement, several examples of such RGO-based applications are presented below.

Flexible field-effect light-emitting diodes based on RGO were fabricated by Wang et al. by employing a graphene field-effect transistor prepared using a laser-based method (Fig. 7a).[154] Researchers have used a semi-RGO light-emitting layer as the interface between the GO and RGO by removing the highly conductive RGO channel (Fig. 7b). Their devices demonstrated bright electroluminescence covering the spectrum from blue to red (Fig. 7c) at the GO/RGO interface. The bright electroluminescence was suggested to be a result of recombination of Poole–Frenkel emission electrons from semi-RGO with holes arriving from the π-band.[154]

Besides field-effect light-emitting diodes, RGO was further employed to fabricate solar cells. Tang et al. have understood that RGO sheets alone cannot be used in dye-sensitized solar cells due to their high defect density and discontinuous structure, which would diminish the RGO photovoltaic potential. Therefore, they have combined RGO with 3D graphene networks and have fabricated dye-sensitized solar cells (DSSCs, schematically depicted in Fig. 7d). Here, the RGO sheets had the role of improving the electron transport at the interfaces between graphene, TiO_2 and the conductive substrate[155] and thus were optimized in terms of mass fraction and degree of reduction. This approach finally led to dye-sensitized solar cells exhibiting a power conversion efficiency of almost 7.7%, a value calculated from the J–V curves shown in Fig. 7e. This efficiency was much higher than the efficiency of dye-sensitized solar cells based on 3D graphene networks or RGO sheets alone.[155] An interesting RGO-based and flexible energy storage integrated device was further reported by Dong et al. They have designed and fabricated a printable dye-sensitized solar cell/supercapacitor integrated energy device exhibiting advantages such as flexibility, portability and high voltage capacity, as demonstrated under various outdoor testing conditions.[156]

The role of RGO in fabrication of optoelectronic devices is actually much broader and it covers several types of solar energy devices. RGO is currently being used in the fabrication of organic,[158–162] perovskite,[163–168] silicon[169–172] or dye-sensitized solar cells.[173–177] In organic and perovskite solar cells RGO is utilized as a component material in fabrication of hole/electron transport layers (or even as a stabilizing agent[167]) while in DSSCs[175–177] and quantum dot-sensitized solar cells (QDSSCs)[173,174] RGO is a composite material for realization of better counter electrodes. RGO can be use alone,[164] doped,[171] coated[172] or in combination with materials such as ZnO sheets[158] or quantum dots,[163] fullerenol,[159] (Au NP:)PEDOT:PSS,[161,162,169] zinc stannate,[165] NiS,[177] NiO,[166] $NiCo_2O_4$,[176] Cu_2S,[174] SnO_2,[168] $CuCo_2O_4$[175] or with multi-walled[160] CNTs.[173] Additional details related to the role of RGO in energy devices can be further consulted in the literature.[178–180]
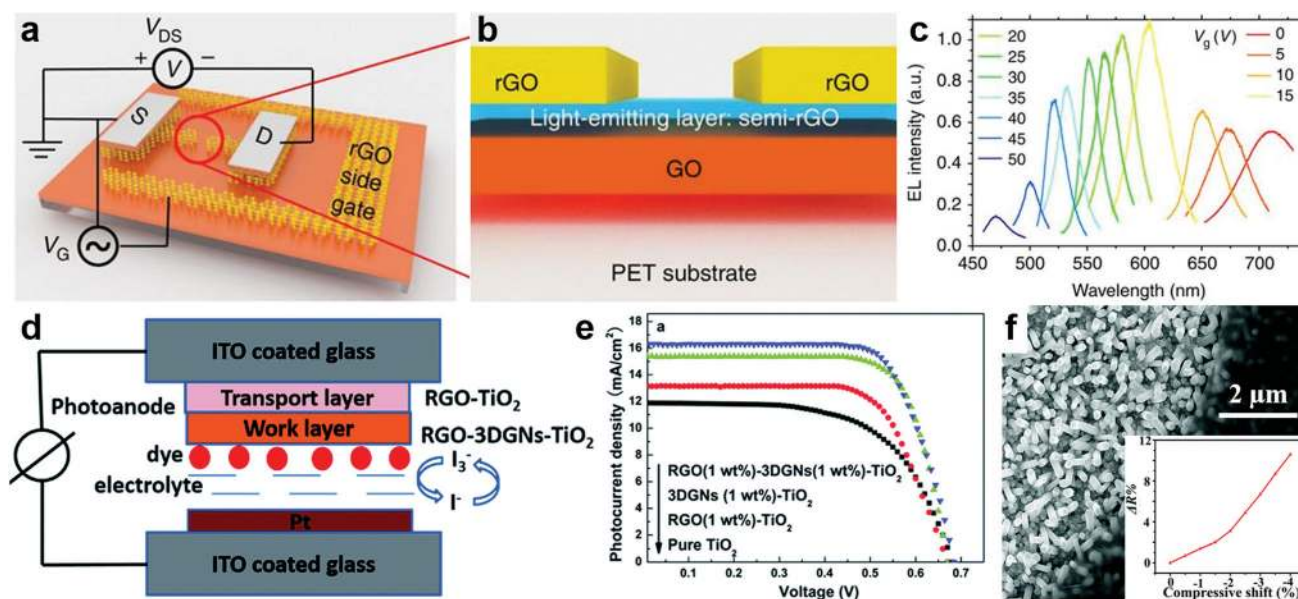

Fig. 7 (a and b) Schematics of the proposed field-effect light-emitting diode. (c) Electroluminescence spectra of the RGO based field-effect light-emitting diode. (d and e) Schematics (d) and J–V curves (e) corresponding to RGO based dye-sensitized solar cells. (f) SEM image of the CdS nanorod array/RGO heterojunction (the inset shows the photoresponsibility change). Adapted with permission from ref. 154 (a–c), ref. 155 (d and e) and ref. 157 (f). Copyright (2015) Macmillan Publishers Limited. Ref. 155 and 157 – published by The Royal Society of Chemistry.

1210 | J. Mater. Chem. C, 2020, **8**, 1198–1224

This journal is © The Royal Society of Chemistry 2020

Photodetectors are another type of devices that could be improved using RGO. Yu *et al.* have fabricated a performant UV-vis-near-infrared (NIR) photodetector based on a CdS nanorod array/RGO film (see Fig. 7f). First, the CdS nanorod array was hydrothermally grown on a conducting substrate. Then, a layer of GO film was spin cast on the CdS array and thermally reduced to RGO. Finally, silver and carbon pastes were used to create two electrodes on the glass conductive substrate and on the RGO film, respectively.[157] The resulting photodetector was able to provide a photoresponse from 365 to 1450 nm. When compared to a single-component CdS nanorod array or RGO film alone, the CdS nanorod array/RGO heterojunction exhibited, under different strains, more than a 10% increase in photoresponsibility (see the inset in Fig. 7f). This was most probably due to the formation of an interfacial Schottky junction between CdS and RGO.[157] Other interesting examples of RGO based optical detectors can be found in the literature.[181]

Furthermore, field-effect transistors,[182,183] memristors,[184] nanomechanical devices[185,186] or various printed electronics[113,187–190] were shown to rely on the use of RGO as well. Although all these examples are very interesting, one case has particularly caught our attention and it is related to 3D printing of RGO nanowires.[190] Kim *et al.* have demonstrated that 3D integrated RGO nanowires with a radius of about 100 nm and possessing various forms can be printed and grown in any direction at specifically selected sites by simply growing GO at the tip of a micropipette followed by reduction. Although a 3D printable size below 10 nm was not achieved, this realization seemed highly effective for the production of future components in RGO-based electrical devices such as stretchable interconnects.[190]

RGO can further be used in applications related to commercial and industrial electronic equipment. Along with tremendous advantages, electronic equipment comes with drawbacks such as electromagnetic interference and/or irradiation resulting from electromagnetic waves, both known to be harmful to human health. Therefore, it is of paramount importance to develop novel materials with enhanced microwave absorption properties that could absorb/attenuate electromagnetic waves. Moreover, such materials could eventually convert the unwanted electromagnetic energy into other types of energy that might be used, for example, to run additional components of specific electronic equipment. Keeping in mind that RGO exhibits efficient absorption properties, Fang *et al.* have prepared 3D RGO powders that could enhance the electromagnetic wave attenuation in the 2–4 GHz range (*i.e.* the S-band).[191] When adding an optimized amount of 3D RGO powder into a paraffin matrix, the 3D RGO exhibited the strongest absorption in the S-band, with the absorption getting stronger when the thickness of the coating was increased. For example, at a thickness of 5 mm the bandwidth of reflection loss was below −5 dB and it could almost cover the whole S-band. These absorption properties were suggested to be inclusively due to the honeycomb-like structure of 3D RGO powders.[191]

A significant reflection loss was reported also for hybrids comprised of CoS_2 nanoparticles that were uniformly embedded into RGO by using a microwave-based hydrothermal method that was capable of avoiding the aggregation of CoS_2 nanoparticles.

Such hybrids demonstrated admirable microwave absorption ability at a rather thin thickness.[192] In this case, for the CoS_2/RGO 1:2 composite (Fig. 8a), a minimum reflection loss of about −57 dB was achieved at 10.9 GHz for a thickness of 2.2 mm, while a reflection loss exceeding −10 dB corresponded to the frequency range between −9 GHz and roughly −13 GHz (Fig. 8b).

A lightweight absorber with superior microwave absorption properties that combines a $Co_{0.33}Ni_{0.67}$ alloy and RGO was recently further prepared by Pan *et al.* They have added $Co_{0.33}Ni_{0.67}$ alloy particles into a colloidal dispersion of GO and have thermally reduced the dispersion at high temperature.[195] Microscopy and spectroscopy measurements indicated that the obtained composite displayed a sandwich-like structure with $Co_{0.33}Ni_{0.67}$ alloy particles being intercalated into the RGO sheets. Here, the maximum reflection loss was measured to be up to −50 dB at a thickness of only 1.8 mm. Moreover, the absorption bandwidth exceeding −10 dB reached up to 14.0 GHz for a thickness range of 5.0–1.4 mm.[195] Interesting microwave absorption properties were further reported in polyaniline coated $Ba_{0.9}La_{0.1}Fe_{11.9}Ni_{0.1}O_{19}$/RGO[196] and RGO coated flaky carbonyl iron (FCI) composites.[197] $Ba_{0.9}La_{0.1}Fe_{11.9}Ni_{0.1}O_{19}$/RGO/polyaniline ternary composites were prepared by *in situ* polymerization and showed a minimum reflection loss of about −49 dB near a frequency of ∼14 GHz with a thickness of 1.9 mm.[196] Instead, coupling FCI and RGO sheets led to homogenous composites that gave a minimum value of reflection loss of about −65 dB at 5.2 GHz when the absorber thickness was almost 3.9 mm.[197]

The last two examples recently reported in the literature illustrate that RGO can be used both as a strong NIR[193] and electromagnetic wave[194] absorber. The first example was given by Hashemi *et al.* who synthesized a novel form of RGO/arginine structure by conjugation of RGO to arginine.[193] Here, the optical absorption of RGO/arginine increased in comparison to that of RGO (Fig. 8c) and the reported results suggested that the RGO/arginine structure was a NIR absorber 3.2 times stronger than GO.[193] The second example was given by Feng *et al.* who used a "coating–coating" route to prepare hierarchically structured $ZnFe_2O_4@SiO_2@RGO$ ternary composites (Fig. 8d). They have then compared the electromagnetic wave absorption properties of these composites with the binary composites of $ZnFe_2O_4@SiO_2$.[194] The authors have observed that the $ZnFe_2O_4@SiO_2@RGO$ composites exhibited enhanced electromagnetic wave absorption properties that could be tuned by inclusively changing the RGO content. After optimization, the minimum reflection loss of the 2.8 mm thick sample could reach about −44 dB at 13.9 GHz (Fig. 8e).[194] Because RGO is a good electromagnetic wave[194] absorber, it can be further employed in realization of composites used in electromagnetic interference (EMI) shielding,[198–204] with a demonstrated shielding effectiveness value of more than 37 dB in the 12.4–18 GHz frequency window, when combined with vertically aligned multiwalled carbon nanotubes.[199] Similar shielding effectiveness, but in the 8.2–12.4 GHz frequency range, was also reported for RGO deposited carbon fiber reinforced polyester composites that were prepared by introducing GO onto the carbon fiber surface through electrophoretic deposition,
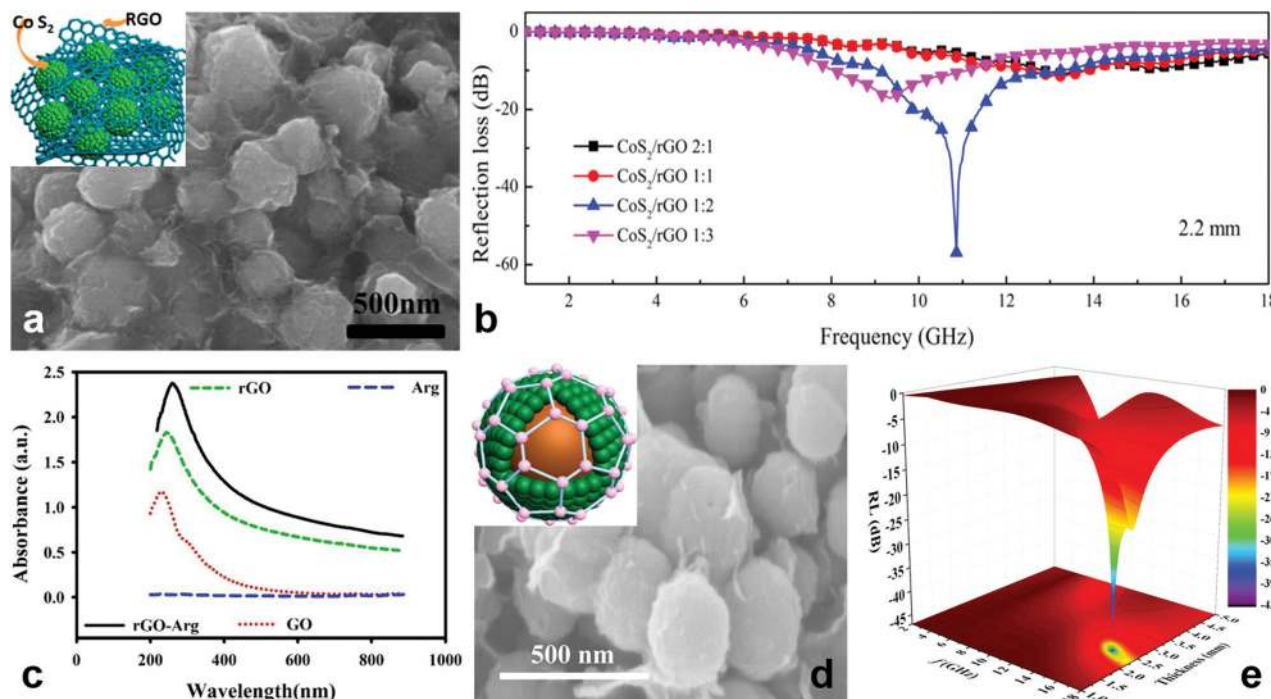
This journal is © The Royal Society of Chemistry 2020

J. Mater. Chem. C, 2020, **8**, 1198–1224 | 1211

Fig. 8 (a) SEM image of the CoS$_2$/RGO 1:2 hybrid along with its schematics. (b) Reflection loss recorded for the CoS$_2$/RGO composite. (c) UV-vis absorption spectra of RGO/arginine, GO, RGO, and arginine. (d) SEM image of the ZnFe$_2$O$_4$@SiO$_2$@RGO composite along with its schematics. (e) 3D representation of the reflection loss of the ZnFe$_2$O$_4$@SiO$_2$@RGO composite. Adapted with permission from ref. 192 (a and b), ref. 193 (c) and ref. 194 (d and e). Copyright (2017) American Chemical Society.

followed by reduction[200] (a value of over 45 dB for the shielding effectiveness measured in the same frequency interval was further reported for composites made of phenolic resin, RGO, γ-Fe$_2$O$_3$ and carbon fibers through a compression molding method[202]).

At the end of this section, we would like to briefly mention that RGO is also used, alone or in various composites, to fabricate optical components with reduced optical loss at high optical intensities known as saturable absorbers (SAs)[205–209] for mode-locking in fiber lasers. Although Sobon *et al.* have shown in 2012 that GO could be used as an efficient SA without the need for its reduction to RGO because both GO and RGO based SAs provided similar results (*i.e.* mode-locked operation with sub-400 fs soliton pulses and a more than 9 nm optical bandwidth at a 1560 nm center wavelength),[205] recently it was demonstrated that RGO shows potential as a SA when it is combined with materials such as tungsten trioxide (WO$_3$)[209] or MoWS$_2$.[208] For instance, Mohanraj *et al.* have combined MoWS$_2$/RGO composites obtained using a hydrothermal exfoliation technique with polyvinyl alcohol (PVA) and have fabricated a film-based SA that led to the first realization of a tunable Q-switched ytterbium-doped fiber laser with a 1 μm wavelength.[208] Other relevant information on RGO-based SAs can be further consulted in the literature.[210,211]

RGO is an ideal material to be used for improvement of catalytic performances

Catalysts have the role of offering repeatedly an alternative reaction mechanism characterized by a lower activation energy,

without being consumed during the ongoing chemical reaction. There are plenty of composite, cluster or hybrid materials that are used as efficient catalysts in various reactions. As we will see below, RGO can be regarded as an attractive component in such materials and it can help improve their catalytic properties.

For instance, Fang *et al.* have taken advantage of the good conductivity of RGO and have fabricated, using pyrolysis and phosphidation, a bimetallic iron–nickel phosphide/RGO (Fe–Ni-P/RGO) composite.[212] After optimization, this porous composite exhibited an oxygen evolution reaction activity that was far superior to, for example, commercial IrO$_2$. Moreover, it highlighted itself as one of the best non-noble metal based catalysts.[212] Remarkably improved catalytic activity for oxygen reduction was further reported by He *et al.* who have anchored on RGO defective CoN$_x$ clusters.[213] This was done by loading very small amounts of porphyrin and Co^{2+} in RGO. The resulting RGO/P/2Co single clusters have demonstrated efficient catalytic performance for the oxygen reduction reaction by exhibiting a half-wave potential almost equal to that of commercial Pt/C.[213] Besides, this potential was superior to most of the other half-wave potentials reported for non-noble metal RGO based catalysts.

The hydrogen evolution reaction is another important process that stays, for example, at the base of hydrogen production through water electrolysis. But here too catalysts are needed to speed up the reaction. One such catalyst for the hydrogen evolution reaction was recently prepared starting from a dispersion containing ammonium molybdate, GO sheets and CNTs *via* spray pyrolysis combined with thermal reduction of GO to RGO.[214] As compared to MoSe$_2$–CNT, MoSe$_2$–RGO and MoSe$_2$ powders,

1212 | *J. Mater. Chem. C*, 2020, **8**, 1198–1224

This journal is © The Royal Society of Chemistry 2020

the MoSe$_2$–RGO–CNT composite powder was better as it exhibited increased catalytic hydrogen evolution reaction activity. This was possible due to the large crystalline active sites that existed in the MoSe$_2$–RGO–CNT composite.[214] Improvement of the hydrogen evolution reaction activity was further targeted by Ni–RGO composite cathodes that were fabricated by Chen *et al.* using an electrodeposition process in supergravity equipment. The resulting Ni–RGO cathodes adopted a hierarchical structure where Ni nanoparticles were densely anchored on the RGO surface and displayed superior catalytic activity inclusively due to the enhanced active surface area.[214]

Ni nanoparticles were further employed as catalyst components by Li *et al.* who decided to reduce their diameter from a few micrometers to some tens of nanometers, to carbon-coat (Fig. 9a) and to anchor the resulting Ni nanoparticles on RGO sheets.[215] The resulting nano-Ni@C/RGO architectures (Fig. 9b) were then tested as H$_2$O$_2$ fuel catalysts in a peroxide–peroxide fuel cell. The reported voltammetry data demonstrated that nano-Ni@C/RGO exhibited an electro-oxidation current density almost 147 times higher than did the Ni microparticles that were embedded in a RGO

matrix (Fig. 9c).[215] Additional interesting examples on this topic can be further examined in the literature.[216]

RGO further proved itself to be a suitable component in fabrication of efficient catalysts that can be used to enhance the catalytic activity for methanol oxidation[217] and rhodamine B (RhB) degradation.[218] For that, Hu *et al.* have attached porous SnO$_2$ hexagonal prisms to Pd-based systems that were placed on an RGO support through co-reduction of PdCl$_4$$^{2-}$ and GO with SnO$_2$ prisms.[217] As a result, both the specific and mass activity towards the oxidation of methanol of the Pd–SnO$_2$/RGO catalyst were enhanced over 1 and 3 times as compared to those of the Pd/RGO catalyst, respectively. This was possible inclusively due to the increased number of more active sites existing in the porous architecture of the SnO$_2$ prisms.[217] In order to boost the photocatalytic activity towards RhB degradation by a 3-fold improvement, Wang *et al.* used RGO as a contact medium and have immobilized sheets of anatase TiO$_2$ on some magnetically actuated 3D cilia films. This significant improvement of the RhB degradation efficiency was observed when the cilia film was optimally actuated by a rotating magnetic field compared to the static situation.[218]

Other RGO-based composites worth mentioning used as catalysts in decomposition of various medicines include RGO–CdS/ZnS,[219] Fe$_3$O$_4$–Mn$_3$O$_4$/RGO[220] and TiO$_2$–RGO.[221] Here, by assembling CdS/ZnS heterostructure nanoparticles on RGO sheets using a hydrothermal method, Tang *et al.* have demonstrated that RGO–CdS/ZnS composites containing 15% RGO showed significant photodegradation of tetracycline antibiotics, most probably because RGO acted as an electron transfer channel to reduce the recombination of electron–hole pairs and thus to enhance the photoconversion efficiency.[219] Instead, a Fe$_3$O$_4$–Mn$_3$O$_4$/RGO composite, prepared by combining a polyol process with an impregnation method, was shown to be a good catalyst for degradation of sulfamethazine in aqueous solution.[220] Although the catalytic mechanism was not clear, the catalytic efficiency for degradation of sulfamethazine of Fe$_3$O$_4$–Mn$_3$O$_4$/RGO was higher than the catalytic efficiency of Fe$_3$O$_4$–Mn$_3$O$_4$ and Mn$_3$O$_4$ catalysts.[220] Furthermore, immobilizing TiO$_2$–RGO composites on optical fibers through a polymer assisted hydrothermal deposition method led to new photocatalysts exhibiting high efficiency in degradation of pharmaceuticals such as carbamazepine, ibuprofen, and sulfamethoxazole. This was possible due to the enhanced utilization efficiency of visible light owing to the reduction of the band energy gap of the TiO$_2$–RGO composites, the latter induced by mixing RGO into TiO$_2$ particles.[221] In this case too, the TiO$_2$–RGO composites displayed much higher photocatalytic activities than pure TiO$_2$ did, which strongly depended on the percentage of RGO in the catalysts.
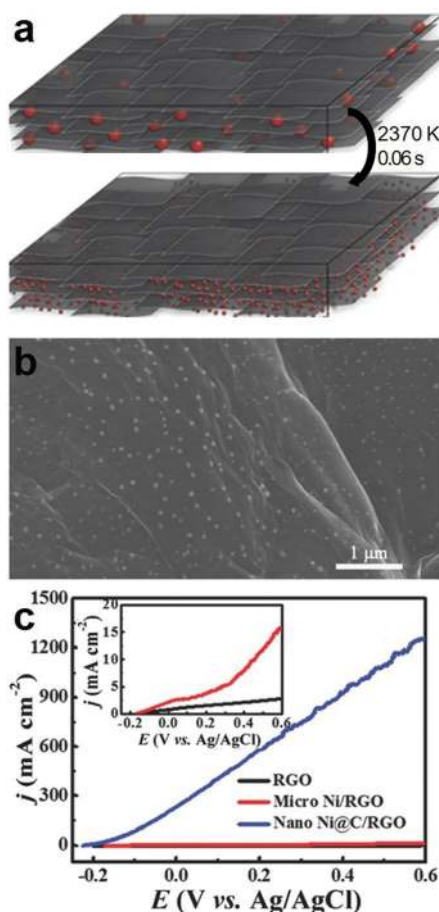

Fig. 9 (a) Schematics of preparation of Ni nanoparticles embedded in carbon layers on RGO sheets from Ni microparticles. (b) SEM micrograph depicting a nano-Ni@C/RGO film. (c) Linear sweep voltammetry curves of various electrodes. Adapted with permission from ref. 215. Copyright (2017) Wiley-VCH Verlag GmbH & Co. KGaA, Weinheim.

Recent bio-applications employing RGO

Generally, RGO defects and edges are functionalised or hydrogen terminated, with the edges being much more reactive than the basal plane. The carboxyl/hydroxyl termination offers a plethora

This journal is © The Royal Society of Chemistry 2020

J. Mater. Chem. C, 2020, **8**, 1198–1224 | **1213**

of routes for further chemical modifications. Additionally, the hydrophobicity of RGO sheets and the possibility of functionalization via π–π stacking utilizing conjugated molecules open up a lot of possibilities for RGO to be used in drug delivery applications. For example, maleimide is a suitable molecule for the functionalization of RGO by hydrophobic interactions using a dopamine ligand (dopa-MAL). It also offers the possibility for covalent functionalization of RGO/dopa-MAL with thiol containing molecules by click reactions. This rationale was adopted by Oz et al. who have clicked RGO/dopa-MAL with a thiol-bearing targeting peptide c(RGDfC) and then further used it in noncovalent loading of anticancer drugs such as doxorubicin (DOX).[222] They have then demonstrated not only that RGO/dopa-MAL-c(RGDfC) was suitable as a drug delivery platform, but also that DOX loaded RGO/dopa-MAL-c(RGDfC) was able to kill cancer cells.[222]

Drug delivery composites based on RGO were further explored by Shao et al. who designed a new composite suitable for chemo-photothermal therapy against cancer. Dopamine was used in this case to reduce GO. RGO functionalized with polydopamine (PDA) (pRGO) was then coated by mesoporous silica (MS) with the aim to enhance the loading of DOX. Further coating with hyaluronic acid (HA) led to a new pRGO@MS(DOX)–HA composite (see the synthetic route in Fig. 10a). Experiments have shown that this composite exhibited improved chemo-photothermal therapy and therapeutic efficacy. This was concluded based on the significantly decreased viability of tumor cells treated with different drug formulations (Fig. 10b), which was not the case for the control groups such as pRGO@MS–HA.[223] Moreover, experiments have further demonstrated the antitumor efficacy of pRGO@MS(DOX)–HA. As we can observe in Fig. 10c, there was significant inhibition of tumor growth in mice that were injected with the pRGO@MS(DOX)–HA composite while irradiated with a NIR laser.[223] The antitumor effect through thermal therapy can also be enhanced by constructing a hydrogel shell directly on cancer cells, from fluorouracil (5-FU, a model anticancer drug),

RGO and Brassica chinensis extract (Bce, a photo-sensitizer used to kill tumor cells by laser radiation).[224] Construction can be realized using self-assembly of GO sheets with Bce. The advantage of this approach is given by the high concentration of drugs that is retained around tumor cells due to rapid gelation of the hydrogel at body temperature.

Besides high-loading drug delivery composites, an efficient drug delivery system also needs a fast drug release mechanism. Being aware of this requirement, Khezri et al. have designed a very fast electrochemical trigger mechanism based on nano-graphene micromachines.[225] The micromachines were fabricated from reduced nanographene oxide (n-RGO), which played the role of a platform for drug delivery, and a platinum (Pt) catalytic layer. The resulting n-RGO/Pt micromachines could be highly loaded with DOX, which was later on efficiently ejected to cancerous cells using an electron injection-based method.[225]

It is worth emphasizing that novel RGO based materials are designed and developed to be used not only in cancer treatment, but also in cancer related fields such as diagnosis and imaging. For example, 'green-corona' G-mNP@RGO composites, with mNPs standing for metallic (Pd, Pt, Ag, and Au) nanoparticles, can be synthesized on RGO sheets using black pepper extract (BPE).[226] Due to their 'green-corona', the G-mNP@rGO composites are able to provide favorable biocompatible surfaces to which antibodies can be attached. Therefore, these composites can be employed both as drug delivery systems and biomarkers in cancer detection. Instead, RGO hybrid complexes of naphthalenediimides (NDI/RGO) can display major potential for bioimaging purposes such as cancer cell imaging.[227]

Yet other examples of RGO based composites used for efficient enzyme immobilization,[228] for stimulating osteoporotic bone regeneration[229] or for sequential enrichment of peptides[230] were recently reported in the literature. For instance, Patel et al. have shown that RGO is able to immobilize enzymes such as laccase and horseradish peroxidase (HRP) utilizing magnetic
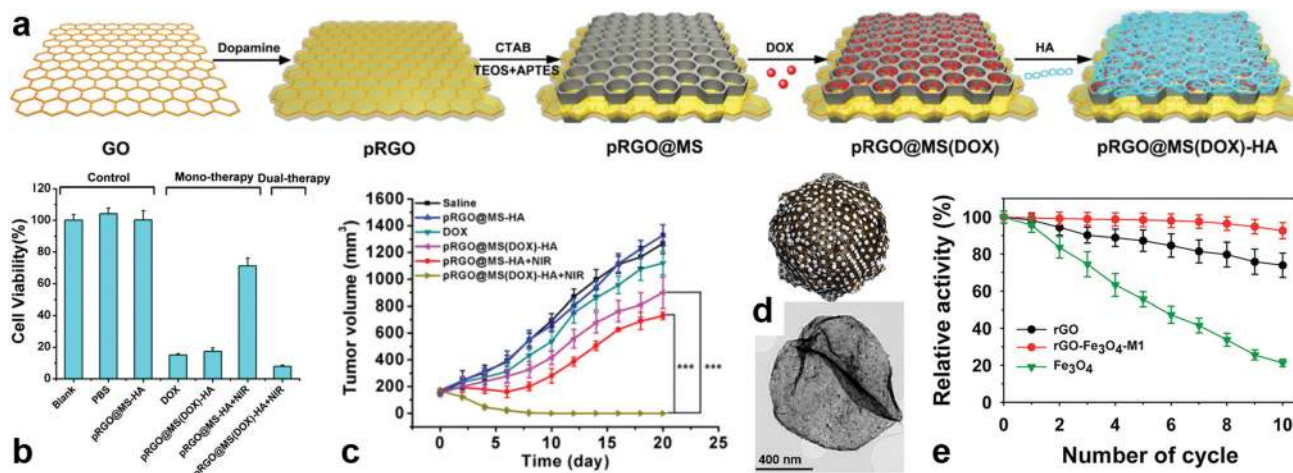

Fig. 10 (a) Schematics depicting the synthesis of the pRGO@MS(DOX)–HA composite. (b) Cell viability of tumor cells treated with various composites with and without NIR laser irradiation for 48 h. (c) Curves depicting tumor growth in mice after receiving various treatments. (d) Schematic representation (top) and TEM image (bottom) of the RGO–Fe_3O_4 composite particles. (e) Reusability of immobilized laccase. Adapted with permission from ref. 223 (a–c) and ref. 228 (d and e). Copyright (2016) American Chemical Society.

RGO–Fe_3O_4 composites of spherical shape (Fig. 10d). Such porous composites were synthesized from Fe_3O_4 containing different percentages of Fe and RGO by employing spray pyrolysis. The RGO–Fe_3O_4 composite containing the highest amount of Fe showed immobilization efficiencies over 110% for laccase and almost 90% for HRP. These values were higher than the immobilization efficiencies corresponding to particles synthesized from pure Fe_3O_4 and RGO.[228] Moreover, laccase immobilized on the RGO–Fe_3O_4 composite containing the highest amount of Fe exhibited over 92% residual activity after 10 cycles of reuse (Fig. 10e).[228]

To stimulate osteoporotic bone regeneration, an electroconductive composite containing RGO, zinc silicate and calcium silicate (RGO/ZS/CS) has been developed using the spin-coating technique. Note that generally Zn plays an important role in bone metabolism, while Si can facilitate calcification of the bone matrix. Mouse bone mesenchymal stem cells (mBMSCs) that were grown on the surface of RGO/ZS/CS experienced an increase of osteogenesis, proving a good mineralization ability of this composite.[229]

To sequentially enrich peptides, a composite from SnO_2 nanorods that were vertically aligned on RGO[230] was constructed by Ma et al. They have exploited the hydrophobicity of RGO and the selectivity of SnO_2 nanorods for phosphopeptide enrichment and have obtained a composite with the ability to sequentially capture endogenous peptides in serum samples.[230]

At the end, we would like to point out that RGO can also be used in realization of micropatterned neuronal networks. Such networks were recently demonstrated on RGO obtained by photo-thermal reduction of GO with a commercial infrared laser.[231] This method led to RGO surfaces with a roughness under the micrometer scale that not only facilitated neuronal adhesion, but also guided neurite outgrowth.[231]

Diversification of environmental applications through the use of RGO based structures

In the present day, it is highly important to develop powerful tools for cleaning and remediation of our more and more polluted environment. Because pollutants are continuously diversifying, researchers have started to design and fabricate, beside classical remediation tools, novel tools for removal of pollutants (including heavy metal ions,[232] organic acids[233] or dyes and bacteria[234]) from the environment. These tools can either be based on chemical functionalization of RGO or can combine RGO with other materials such as montmorillonite (MMT). For example, Awad et al. have fabricated a novel chelating adsorbent by chemically modifying GO through functionalization of amidinothiourea to finally form 2-imino-4-thiobiuret-partially reduced graphene oxide (IT-PRGO). IT-PRGO demonstrated its capability in removal of several toxic metal ions including Hg(II), Pb(II), Cr(VI), Cu(II) and As(V) from wastewater, with maximum sorption capacities of about 624 mg g^{-1}, 101 mg g^{-1}, 63 mg g^{-1}, 37 mg g^{-1} and 19 mg g^{-1}, respectively.[232] Moreover, IT-PRGO displayed

100% removal of Hg(II) at concentrations up to 100 ppm. Most probably this was possible due to a chemisorption mechanism triggered by the amidinothiourea groups attached to RGO sheets.[232]

Functionalization of RGO using an iron salt was further employed to coat sand and to use it as an adsorbent of fulvic acid (FA). FA is an important component of natural organic matter that can be found in wastewater and that is harmful to humans because it can lead, for example, to trihalomethanes. The results have indicated that the FA adsorption efficacy of functionalized RGO was higher compared to that of powder activated carbon. This better efficacy was suggested to be inclusively a result of the π–π interactions between the carbons of FA and functionalized RGO.[233] Wastewater treatment was further targeted by Zhang et al. who have proposed a cheap yet recyclable wastewater purification aerogel. This gel was synthesized from RGO and MMT and possessed both a 3D structure and good mechanical strength.[234] The RGO–MMT aerogel has not only displayed high removal efficiencies for methylene blue (MB, over 97%) and Cr(VI) (almost 95%), but it has also shown interesting antibacterial activity against both Escherichia coli and Staphylococcus aureus.[234]

Improving the quality of the environment can be further implemented through degradation of pollutants, by combining RGO with In_2O_3 and Cu_2O materials. For that, researchers have created shape controlled Cu_2O/RGO/In_2O_3 hybrids (Fig. 11a) containing abundant oxygen vacancies that can supply high catalytic capacity. The advantage of the Cu_2O/RGO/In_2O_3 hybrid as compared to the pure In_2O_3 and Cu_2O materials lies in its capacity to photodegrade pollutants such as Cr^{6+} and MB.[235] For example, the Cu_2O/RGO/In_2O_3 hybrid exhibited a degradation efficiency of Cr^{6+} of over 95% after illumination for 6 h (Fig. 11b). Degradation of Cr^{6+} and MB was possible due to a rather complex mechanism that is schematically depicted in Fig. 11c. Here, the new interfaces formed between In_2O_3 and Cu_2O led to the appearance of diffusive electronic states in the Cu_2O/RGO/In_2O_3 hybrid, while the transfer and distribution of charges onto the RGO sheets increased the oxidation potential of this hybrid.[235]

Yet another efficient way to remediate the polluted environment is based on bio-reduction of arsenic (As) and iron (Fe) from soil. As shown by Chen et al., this is feasible when using a composite made of anthraquinone-2,6-disulphonate (AQDS) and RGO. Adding the AQDS–RGO composite into acetate was shown to improve the release of As(III) and Fe(II) from arsenic-rich soil as compared to pure acetate. Moreover, increasing the AQDS content in the AQDS–RGO composites facilitated bio-reduction of As(V).[236]

RGO based structures for fabrication of membranes

Membranes are filtering tools used to separate various components in a whole range of applications such as osmosis, separation of oil from water, water desalinization, etc. Due to its mechanical strength, atomic thickness, large surface area and chemical resistance,
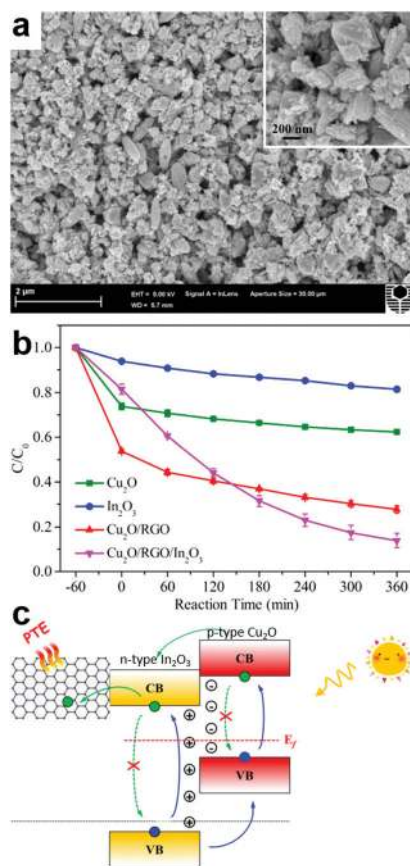
Fig. 11 (a) SEM image of the $Cu_2O/RGO/In_2O_3$ hybrid. The inset represents a magnification of (a). (b) Photocatalytic reduction of Cr^{6+} when employing different catalysts. (c) Mechanism depicting the separation of electron–hole pairs on the $Cu_2O/RGO/In_2O_3$ hybrid. Adapted with permission from ref. 235. Copyright (2017) American Chemical Society.

An interesting internal architecture inspired by mussels was further designed by Zhu et al. who realized a high-flux nano-filtration membrane possessing high surface hydrophobicity.[239] Such a membrane was prepared by co-depositing RGO–copper composites, synthesized via in situ reduction with PDA, onto an ultrafiltration support. The resulting PDA–RGO–copper layer was able to not only facilitate high water permeability, but also to provide good separation properties for dye purification or desalination.[239]

At the end of this section, we would like to briefly mention the key role of RGO in photoelectrochemical bipolar membranes[240] that can be used for solar water splitting under specific pH conditions and light absorbers used in solar thermal steam generation.[241] For instance, because RGO can be easily tuned via various chemical procedures, it becomes an ideal material for the realization of the interfacial layer between photoelectrodes, a critical component in bipolar membranes with the role of transporting negative and positive charges through the ion-exchange layers to the alkaline anode and acidic cathode, respectively. In this way, bipolar membranes can maintain a pH gradient for optimal reaction conditions by the dissociation of water.[240] Instead, for realization of efficient RGO-based light absorbers, Yang et al. have further functionalized RGO using hydrophilic groups. The reported results showed that, under specific illumination conditions, functionalized RGO could improve the overall solar-to-vapor efficiency from 38% to 48% compared to RGO due to a surface effect mainly attributed to the higher hydrophilicity of functionalized RGO.[241]

Mechanical and rheological applications utilizing RGO structures

When mixed with other materials, RGO can induce specific ordering and orientation of molecules in the resulting composites leading to altered mechanical properties. For example, Colonna et al. have prepared polymer composites by polymerization of cyclic butylene terephthalate into poly(butylene terephthalate) (pCBT) in the presence of RGO. They have then observed that the inclusion of RGO flakes dramatically affected the crystallization of pCBT by increasing both the crystallization temperature and crystallization rate.[242] The crystallization rate increased most probably due to strong nucleation induced by the RGO flakes. Moreover, experiments have indicated that there was a strong interfacial interaction between the aromatic rings of pCBT and RGO. This result could be extremely useful, for example, when fabricating composite interfaces with specific stress transfer.[242] Crystallization was further used to influence the mechanical properties of high density polyethylene (HDPE)/RGO composite bars.[243] The reported results demonstrated again that the use of RGO led to better mechanical properties of HDPE because it affected the nucleation of HDPE.

Furthermore, the mechanical properties of RGO were reported to be responsible for the improved performances of cement composites. Gholampour et al. have prepared RGO samples with different levels of oxygen groups (Fig. 13a) and have mixed them

RGO can be combined with other materials to improve the overall performance of certain membranes. Wang et al. have recently used the concept of stacked RGO laminate membranes (Fig. 12a) and have shown that multilayer membranes (Fig. 12b) can be prepared by controlling the assembly of RGO laminates.[237] To do so, the authors have firstly filtered RGO dispersions on a polyvinylidene fluoride membrane. Then, they have induced a cross-linking reaction by filtering hydrochloric acid through the RGO membrane and by adding it onto the membrane at high temperature. The resulting RGO laminate membrane was comprised of interconnected nanochannels in hydrophilic interlayer regions and hydrophobic walls and it could be used to transport water molecules. Interestingly, the water permeation/flux was higher in membranes that were prepared using RGO with a medium reduction degree (Fig. 12c).[237] Jia et al. have further used the assembly process to construct ionic nanochannels in Nafion slightly reduced graphene oxide membranes (N-sRGO) by exploiting the dependence of the self-assembly of the amphiphilic Nafion in water on the concentration. The optimized N-sRGO membranes exhibited, under the same conditions, a nearly 4-fold higher proton conductivity compared to that of the commercial Nafion membrane (Fig. 12d).[238]

1216 | J. Mater. Chem. C, 2020, 8, 1198–1224

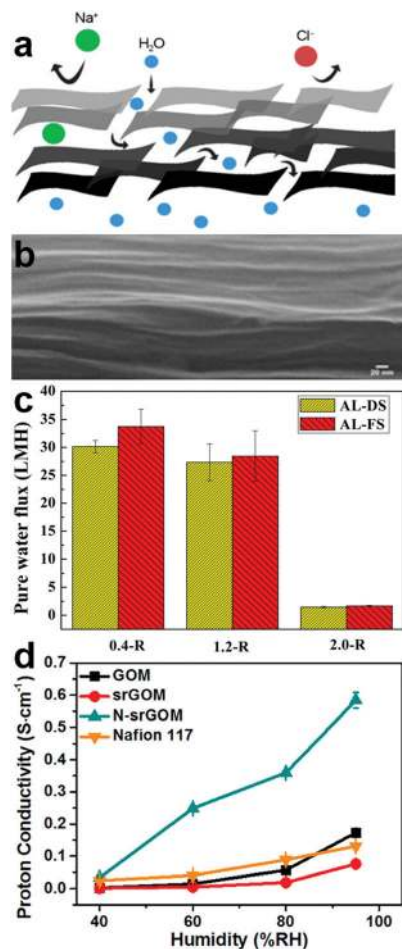This journal is © The Royal Society of Chemistry 2020

Fig. 12 (a and b) Schematics (a) and SEM cross-section (b) depicting a stacked RGO laminate membrane. (c) Water flux. (d) Dependence of proton conductivity on humidity. Adapted with permission from ref. 237 (a–c) and ref. 238 (d). Copyright (2017) American Chemical Society.
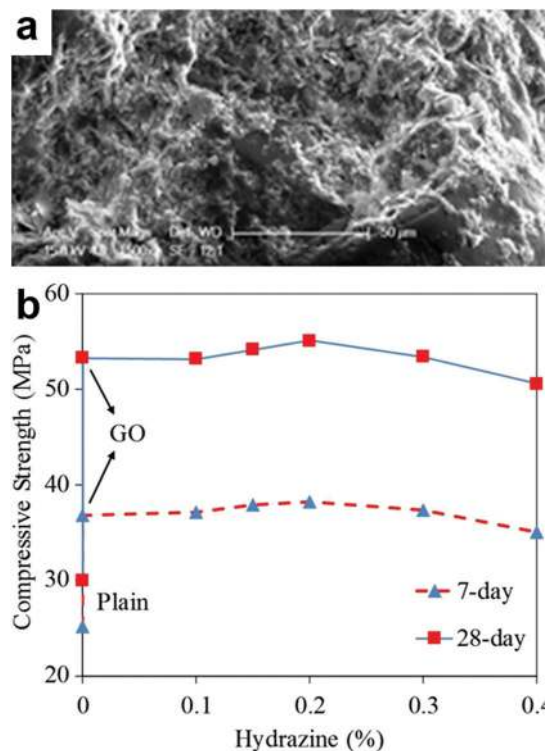

Fig. 13 (a) SEM image of RGO with high density levels of oxygen groups. (b) Variation of the 7 day and 28 day compressive strengths of RGO/cement mortar. Adapted with permission from ref. 244. Copyright (2017) American Chemical Society.

with cement using an optimal dosage of 0.1% RGO.[244] Measurements have revealed that the oxygen level of RGO had a significant influence on the mechanical properties of cement because the right level of oxygen groups on RGO sheets could ensure sufficient bonding between the calcium silicate hydrate components in the cement matrix. Moreover, in comparison with the plain cement mortar, the use of RGO containing a mild level of oxygen groups led to a notable strength enhancement of over 83% in the 28 day compressive strength (Fig. 13b). This mortar enhancement was attributed inclusively to the higher crystallinity of the graphene structures.[244] Other work describing mechanical and/or thermal properties of RGO-based cement composites can be further consulted in the literature.[245,246] Moreover, a number of studies have shown that RGO can not only reinforce materials and improve their strength, but also can introduce multifunctionality in the form of EMI shielding[200] and microwave absorption properties,[247,248] demonstrating the ability of RGO to deliver multifunctional improvements that cut across different application sectors.

The thermomechanical properties of some materials can also be improved using RGO. For instance, Tiwari et al. have manipulated the dispersion of RGO in polycarbonate/nylon-based composites.

This was done by varying the mixing-sequence of RGO in the polymer matrix under specific shear pressure conditions. The obtained hybrid systems were shown to achieve enhanced mechanical, chemical and thermal properties.[249] According to rheological measurements, this was possible inclusively due to advantageous localization of RGO in the nylon phase, which actually influenced the nylon crystallization. Enhanced mechanical and thermal properties that exceed those of synthetic plastics were recently further reported for a class of green plastics fabricated from cellulose and RGO.[250] Here, a thermal conductivity enhanced to 9.0 W m^{-1} K^{-1} with 6 weight% RGO loading was reported. This enhancement was suggested to be caused by several contributions, including strong hydrogen bonding interactions between cellulose and RGO as well as uniform dispersion of RGO within the green plastic.[250]

Yet other applications based on the mechanical properties of RGO, including aerospace or military industries, were reported in the literature.[251,252] RGO can be used along with polyester (PES) to fabricate composites containing woven Kevlar fiber (WKF).[251] Hazarika et al. have realized WKF/NiCo$_2$S$_4$/RGO/PES composites by hydrothermal synthesis of aligned NiCo$_2$S$_4$ nanowires on the surface of WKF that have been dispersed along with RGO in PES resin. In comparison to the bare WKF/PES, the WKF/NiCo$_2$S$_4$/RGO/PES composite exhibited a tensile strength enhanced by over 96%.[251] Furthermore, RGO can also be employed along with GO and hexachlorocyclotriphosphazene (HCCP) aqueous pulp to realize flame retardant graphene paper.

RGO–HCCP paper could have huge potential in applications related to military and aerospace flame retardant fields because such paper was found to be able to maintain its structure intact in an ethanol flame for a longer time than did the paper made of GO.[252]

Advantages of employing RGO in anticorrosion and lubrication applications

Corrosion is a natural process that occurs generally in metals, although it can also occur in ceramics and polymers, and degrades a metal into its oxidized, hydroxidized or sulfidized forms. Rusting is just one of many examples of corrosion that produce costly damage in many branches of world-wide industry dealing with surfaces and interfaces. Therefore, corrosion protection is a highly important technological branch that needs strategies to decelerate the kinetics and to restrict the mechanisms of corrosion. RGO represent a viable material that can be combined with other polymeric[253] or ZnAl based layered double hydroxides (LDH)[254] to obtain composites of enhanced anticorrosion performance.

For instance, Xiao *et al.* have used RGO, polyvinylidene difluoride (PVDF) and polyurethanes (PU) to fabricate an anticorrosion composite possessing a sandwich-like structure. Their results have shown that the addition of PU and of the right amount of RGO significantly improved the anticorrosion
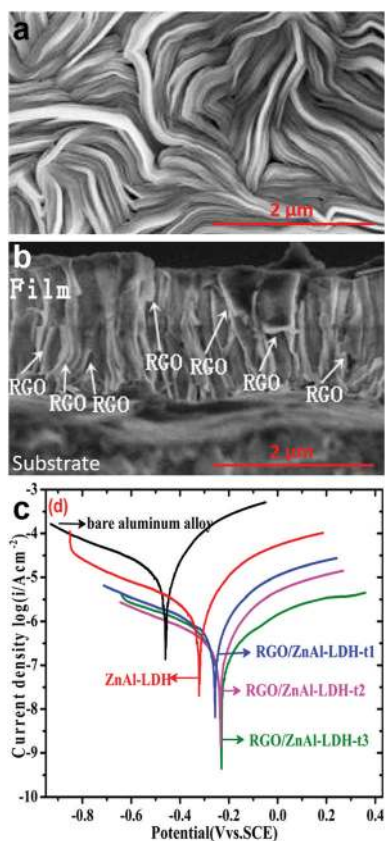

Fig. 14 (a and b) Top (a) and cross-sectional (b) SEM view of an RGO/ZnAl-LDH film composite. (c) Potentiodynamic polarization curves of RGO/ZnAl-LDH films immersed for 7 days in NaCl solution. Adapted with permission from ref. 254. Copyright (2017) American Chemical Society.

performance of the bare PVDF coating, both in terms of corrosion potential and protection efficiency.[253] These enhancement effects were attributed to the hydrophobic property and to the high-aspect ratio of RGO in the PVDF matrix, which have obstructed diffusion of corrosion-generating molecules.[253]

Luo *et al.* have further prepared hybrid RGO/ZnAl-LDH composite films (Fig. 14a and b) using a hydrothermal continuous flow method that has allowed them to directly grow the composite on the surface of the Al alloy substrate.[254] A comprehensive analysis of the potentiodynamic polarization curves recorded using electrochemical measurements (Fig. 14c) has revealed that, in comparison to the ZnAl-LDH film, the RGO/ZnAl-LDH film significantly enhanced the corrosion protection. Because RGO limited the diffusion of molecules such as water or oxygen in the RGO/ZnAl-LDH films, these composite films could maintain good corrosion resistance even after 7 days of immersion in a highly concentrated NaCl solution.[254]

Besides its anticorrosion properties, RGO can also be used as a lubricant additive in various oil dispersions. An example in this direction was recently given by Zhao *et al.* who synthesized RGO using a cost-effective synthesis method based on mild thermal reduction of GO.[255] TEM and X-ray photoelectron spectroscopy have revealed that RGO adopted a rather ordered lamellar structure in oil dispersions. When compared to the base oil dispersions, the RGO containing oil dispersion exhibited a friction coefficient reduced by 30%, along with fewer scratches on the rubbing surfaces.[255]

Conclusions

Due to its astonishing graphene-like properties and a variety of rather facile synthesis routes leading to decent amounts, RGO is proving itself to be a highly versatile material in many technological branches and it is finding use in more and more devices and applications. From the examples presented in this work, we conclude that in most applications RGO should be predominantly used as a component in binary, ternary or quaternary composites. The advantage of preparing such composites is double. Firstly, RGO based composites of complex, often hierarchical architectures exhibit various novel and/or enhanced structure-related properties and can be prepared rather easily from different precursor structures (sheets, rods, ribbons, wires, needles, particles, spheres, prisms, *etc.*) using various synthetic and/or physical methods (chemical/thermal reactions, pyrolysis, functionalization, polymerization, doping, hybridization, cross-linking, dispersion and self-assembly, seeding, nucleation and growth, *etc.*). Secondly, synergistic effects resulting from the coupling between various composite components abound in variety and are generally highly beneficial. An increased number of positive synergistic effects could especially be identified in multicomponent composites used for sensors as well as in mechanical, rheological and anti-corrosion applications. Moreover, we have noticed that, for fabrication of efficient batteries in particular, RGO based composites had to be porous and had to possess a 3D structure. These conditions facilitated charge transfer and improved ion diffusion processes.

To bring RGO to its full potential, novel methods of synthesis and processing need to be further designed and developed in order to widen and/or further improve its set of properties. For example, in the future, RGO could be regarded as an essential material component in organic flexible optoelectronic devices as well as in polymer-based composites if a novel synthetic route that could lead to highly concentrated RGO suspensions in organic solvents could be imagined, designed and experimentally implemented.

Conflicts of interest

There are no conflicts to declare.

Acknowledgements

References

1 P. R. Wallace, *Phys. Rev.*, 1947, **71**, 622–634.

2 K. S. Novoselov, A. K. Geim, S. V. Morozov, D. Jiang, Y. Zhang, S. V. Dubonos, I. V. Grigorieva and A. A. Firsov, *Science*, 2004, **306**, 666–669.

3 A. K. Geim and K. S. Novoselov, *Nat. Mater.*, 2007, **6**, 183–191.

4 C. Lee, X. Wei, J. W. Kysar and J. Hone, *Science*, 2008, **321**, 385–388.

5 K. I. Bolotin, K. J. Sikes, Z. Jiang, M. Klima, G. Fudenberg, J. Hone, P. Kim and H. L. Stormer, *Solid State Commun.*, 2008, **146**, 351–355.

6 A. K. Geim, *Science*, 2009, **324**, 1530–1534.

7 R. Garg, S. Elmas, T. Nann and M. R. Andersson, *Adv. Energy Mater.*, 2017, **7**, 1601393.

8 M. Xu, J. Qi, F. Li, X. Liao, S. Liu and Y. Zhang, *RSC Adv.*, 2017, **7**, 30506–30512.

9 B. C. Thompson, E. Murray and G. G. Wallace, *Adv. Mater.*, 2015, **27**, 7563–7582.

10 X. Shuai, Z. Bo, J. Kong, J. Yan and K. Cen, *RSC Adv.*, 2017, **7**, 2667–2675.

11 C. Tang, B.-Q. Li, Q. Zhang, L. Zhu, H.-F. Wang, J.-L. Shi and F. Wei, *Adv. Funct. Mater.*, 2016, **26**, 577–585.

12 E. Kecsenovity, B. Endrődi, P. S. Tóth, Y. Zou, R. A. W. Dryfe, K. Rajeshwar and C. Janáky, *J. Am. Chem. Soc.*, 2017, **139**, 6682–6692.

13 D. G. Cahill, P. V. Braun, G. Chen, D. R. Clarke, S. Fan, K. E. Goodson, P. Keblinski, W. P. King, G. D. Mahan, A. Majumdar, H. J. Maris, S. R. Phillpot, E. Pop and L. Shi, *Appl. Phys. Rev.*, 2014, **1**, 011305.

14 J.-H. Lee, P. E. Loya, J. Lou and E. L. Thomas, *Science*, 2014, **346**, 1092–1096.

15 Z. Liu, Y. Chen, W. Dai, Y. Wu, M. Wang, X. Hou, H. Li, N. Jiang, C.-T. Lin and J. Yu, *RSC Adv.*, 2018, **8**, 1065–1070.

16 M. Buzaglo, M. Shtein, S. Kober, R. Lovrinčić, A. Vilan and O. Regev, *Phys. Chem. Chem. Phys.*, 2013, **15**, 4428–4435.

17 M. Buzaglo, I. P. Bar, M. Varenik, L. Shunak, S. Pevzner and O. Regev, *Adv. Mater.*, 2017, **29**, 1603528.

18 K. R. Paton, E. Varrla, C. Backes, R. J. Smith, U. Khan, A. O'Neill, C. Boland, M. Lotya, O. M. Istrate, P. King, T. Higgins, S. Barwich, P. May, P. Puczkarski, I. Ahmed, M. Moebius, H. Pettersson, E. Long, J. Coelho, S. E. O'Brien, E. K. McGuire, B. M. Sanchez, G. S. Duesberg, N. McEvoy, T. J. Pennycook, C. Downing, A. Crossley, V. Nicolosi and J. N. Coleman, *Nat. Mater.*, 2014, **13**, 624–630.

19 B. Marta, C. Leordean, T. Istvan, I. Botiz and S. Astilean, *Appl. Surf. Sci.*, 2016, **363**, 613–618.

20 C. Berger, Z. Song, X. Li, X. Wu, N. Brown, C. Naud, D. Mayou, T. Li, J. Hass, A. N. Marchenkov, E. H. Conrad, P. N. First and W. A. de Heer, *Science*, 2006, **312**, 1191–1196.

21 P. W. Sutter, J.-I. Flege and E. A. Sutter, *Nat. Mater.*, 2008, **7**, 406–411.

22 L. Jiao, L. Zhang, X. Wang, G. Diankov and H. Dai, *Nature*, 2009, **458**, 877–880.

23 K. Soumen, V. K. Naveen, B. N. Ashok, P. L. Niranjan, M. Ratikant, V. G. Sathe, S. V. Bhoraskar and A. K. Das, *J. Phys. D: Appl. Phys.*, 2009, **42**, 115201.

24 W. Ren and H.-M. Cheng, *Nat. Nanotechnol.*, 2014, **9**, 726–730.

25 G. Eda and M. Chhowalla, *Adv. Mater.*, 2010, **22**, 2392–2415.

26 S. Sajjad, S. A. Khan Leghari and A. Iqbal, *ACS Appl. Mater. Interfaces*, 2017, **9**, 43393–43414.

27 A. Agresti, S. Pescetelli, L. Cinà, D. Konios, G. Kakavelakis, E. Kymakis and A. D. Carlo, *Adv. Funct. Mater.*, 2016, **26**, 2686–2694.

28 J. Liu, M. Xu, B. Wang, Z. Zhou and L. Wang, *RSC Adv.*, 2017, **7**, 1432–1438.

29 Z. Li, S. Gadipelli, Y. Yang and Z. Guo, *Small*, 2017, **13**, 1702474.

30 S. Baek, J. Oh, J. Song, H. Choi, J. Yoo, G.-Y. Park, J. Han, Y. Chang, H. Park, H. Kim, S.-G. Cho, B.-S. Kim and J. Kim, *Small*, 2017, **13**, 1601993.

31 X. Tian, Z. Yang, G. Duan, A. Wu, Z. Gu, L. Zhang, C. Chen, Z. Chai, C. Ge and R. Zhou, *Small*, 2017, **13**, 1602133.

32 M. Zhang, N. Zhou, P. Yuan, Y. Su, M. Shao and C. Chi, *RSC Adv.*, 2017, **7**, 9284–9293.

33 K. M. Kang, D. W. Kim, C. E. Ren, K. M. Cho, S. J. Kim, J. H. Choi, Y. T. Nam, Y. Gogotsi and H.-T. Jung, *ACS Appl. Mater. Interfaces*, 2017, **9**, 44687–44694.

34 C. Li, Z.-Y. Wu, H.-W. Liang, J.-F. Chen and S.-H. Yu, *Small*, 2017, **13**, 1700453.

35 C. Zhu, P. Liu and A. P. Mathew, *ACS Appl. Mater. Interfaces*, 2017, **9**, 21048–21058.

36 W. S. Hummers and R. E. Offeman, *J. Am. Chem. Soc.*, 1958, **80**, 1339.

37 L. Staudenmaier, *Ber. Dtsch. Chem. Ges.*, 1898, **31**, 1481–1487.

38 B. C. Brodie, *Philos. Trans. R. Soc. London*, 1859, **149**, 249–259.

39 C.-Y. Su, A.-Y. Lu, Y. Xu, F.-R. Chen, A. N. Khlobystov and L.-J. Li, *ACS Nano*, 2011, **5**, 2332–2339.

40 J. Cao, P. He, M. A. Mohammed, X. Zhao, R. J. Young, B. Derby, I. A. Kinloch and R. A. W. Dryfe, *J. Am. Chem. Soc.*, 2017, **139**, 17446–17456.

41 B. Liu, J. Xie, H. Ma, X. Zhang, Y. Pan, J. Lv, H. Ge, N. Ren, H. Su, X. Xie, L. Huang and W. Huang, *Small*, 2017, **13**, 1601001.

42 M. Iliut, A.-M. Gabudean, C. Leordean, T. Simon, C.-M. Teodorescu and S. Astilean, *Chem. Phys. Lett.*, 2013, **586**, 127–131.

43 M. Iliut, C. Leordean, V. Canpean, C.-M. Teodorescu and S. Astilean, *J. Mater. Chem. C*, 2013, **1**, 4094–4104.

44 S. J. An, Y. Zhu, S. H. Lee, M. D. Stoller, T. Emilsson, S. Park, A. Velamakanni, J. An and R. S. Ruoff, *J. Phys. Chem. Lett.*, 2010, **1**, 1259–1263.

45 S. Pei and H.-M. Cheng, *Carbon*, 2012, **50**, 3210–3228.

46 F. Iskandar, U. Hikmah, E. Stavila and A. H. Aimon, *RSC Adv.*, 2017, **7**, 52391–52397.

47 Y. Zhang, L. Guo, S. Wei, Y. He, H. Xia, Q. Chen, H.-B. Sun and F.-S. Xiao, *Nano Today*, 2010, **5**, 15–20.

48 D. Zhan, Z. Ni, W. Chen, L. Sun, Z. Luo, L. Lai, T. Yu, A. T. S. Wee and Z. Shen, *Carbon*, 2011, **49**, 1362–1366.

49 R. Ma and V. V. Tsukruk, *Adv. Funct. Mater.*, 2017, **27**, 1604802.

50 P. Kumar, K. S. Subrahmanyam and C. N. R. Rao, *Int. J. Nanosci.*, 2011, **10**, 559–566.

51 M. Mohandoss, S. S. Gupta, A. Nelleri, T. Pradeep and S. M. Maliyekkal, *RSC Adv.*, 2017, **7**, 957–963.

52 W. Gao, L. B. Alemany, L. Ci and P. M. Ajayan, *Nat. Chem.*, 2009, **1**, 403–408.

53 S. Stankovich, D. A. Dikin, G. H. B. Dommett, K. M. Kohlhaas, E. J. Zimney, E. A. Stach, R. D. Piner, S. T. Nguyen and R. S. Ruoff, *Nature*, 2006, **442**, 282–286.

54 H.-J. Shin, K. K. Kim, A. Benayad, S.-M. Yoon, H. K. Park, I.-S. Jung, M. H. Jin, H.-K. Jeong, J. M. Kim, J.-Y. Choi and Y. H. Lee, *Adv. Funct. Mater.*, 2009, **19**, 1987–1992.

55 I. K. Moon, J. Lee, R. S. Ruoff and H. Lee, *Nat. Commun.*, 2010, **1**, 73.

56 M. J. Fernández-Merino, L. Guardia, J. I. Paredes, S. Villar-Rodil, P. Solís-Fernández, A. Martínez-Alonso and J. M. D. Tascón, *J. Phys. Chem. C*, 2010, **114**, 6426–6432.

57 X. Wang, L. Zhi and K. Müllen, *Nano Lett.*, 2008, **8**, 323–327.

58 X. Xie, Y. Zhou and K. Huang, *Front. Chem.*, 2019, **7**, 355.

59 S.-H. Park and H.-S. Kim, *Nanotechnology*, 2015, **26**, 205601.

60 K. F. Mak, L. Ju, F. Wang and T. F. Heinz, *Solid State Commun.*, 2012, **152**, 1341–1349.

61 Y. Shen, S. Yang, P. Zhou, Q. Sun, P. Wang, L. Wan, J. Li, L. Chen, X. Wang, S. Ding and D. Wei Zhang, *Carbon*, 2013, **62**, 157–164.

62 D. A. Sokolov, Y. V. Morozov, M. P. McDonald, F. Vietmeyer, J. H. Hodak and M. Kuno, *Nano Lett.*, 2014, **14**, 3172–3179.

63 R. Su, S. F. Lin, D. Q. Chen and G. H. Chen, *J. Phys. Chem. C*, 2014, **118**, 12520–12525.

64 Y. Guo, X. Sun, Y. Liu, W. Wang, H. Qiu and J. Gao, *Carbon*, 2012, **50**, 2513–2523.

65 J. Li, G. Xiao, C. Chen, R. Li and D. Yan, *J. Mater. Chem. A*, 2013, **1**, 1481–1487.

66 S. Liu, J. Tian, L. Wang and X. Sun, *Carbon*, 2011, **49**, 3158–3164.

67 B. Zhang, W. Ning, J. Zhang, X. Qiao, J. Zhang, J. He and C.-Y. Liu, *J. Mater. Chem.*, 2010, **20**, 5401–5403.

68 S. Liu, L. Wang, J. Tian, Y. Luo, X. Zhang and X. Sun, *J. Colloid Interface Sci.*, 2011, **363**, 615–619.

69 T. K. Das, P. Bhawal, S. Ganguly, S. Mondal and N. C. Das, *Surf. Interfaces*, 2018, **13**, 79–91.

70 A. Chae, S. Jo, Y. Choi, B. Ryu, C. A. Choi, S. Y. Park and I. In, *Appl. Surf. Sci.*, 2019, **474**, 111–117.

71 J. Li, J.-c. Cui, Z.-z. Yang, H.-x. Qiu, Z.-h. Tang and J.-h. Yang, *New Carbon Mater.*, 2018, **33**, 19–25.

72 X. Zhao, M. Gnanaseelan, D. Jehnichen, F. Simon and J. Pionteck, *J. Mater. Sci.*, 2019, **54**, 10809–10824.

73 P. Lin, Q. Yan, Y. Chen, X. Li and Z. Cheng, *Chem. Eng. J.*, 2018, **334**, 1023–1033.

74 J. E. Ellis, D. C. Sorescu, S. C. Burkert, D. L. White and A. Star, *ACS Appl. Mater. Interfaces*, 2017, **9**, 27142–27151.

75 A. Shanmugasundaram, V. Gundimeda, T. Hou and D. W. Lee, *ACS Appl. Mater. Interfaces*, 2017, **9**, 31728–31740.

76 V. Chivukula, C. Kritzinger, F. Yavari, D. Čiplys, N. Koratkar and M. S. Shur, Detection of CO_2 absorption in graphene using surface acoustic waves, 2010 IEEE International Ultrasonics Symposium, 2010, pp. 257–260.

77 Y. Xia, J. Wang, J.-L. Xu, X. Li, D. Xie, L. Xiang and S. Komarneni, *ACS Appl. Mater. Interfaces*, 2016, **8**, 35454–35463.

78 S. Thomas, M. Cole, A. De Luca, F. Torrisi, A. C. Ferrari, F. Udrea and J. W. Gardner, *Procedia Eng.*, 2014, **87**, 999–1002.

79 X. Xia, S. Guo, W. Zhao, P. Xu, H. Yu, T. Xu and X. Li, *Sens. Actuators, B*, 2014, **202**, 846–853.

80 D. Zaharie-Butucel, L. Digianantonio, C. Leordean, L. Ressier, S. Astilean and C. Farcau, *Carbon*, 2017, **113**, 361–370.

81 H. Yu, P. Xu, D. W. Lee and X. Li, *J. Mater. Chem. A*, 2013, **1**, 4444–4450.

82 C. Li, T. Zhang, J. Zhao, H. Liu, B. Zheng, Y. Gu, X. Yan, Y. Li, N. Lu, Z. Zhang and G. Feng, *ACS Appl. Mater. Interfaces*, 2017, **9**, 2984–2994.

83 D. Čiplys, R. Rimeika, V. Chivukula, M. S. Shur, J. H. Kim and J. M. Xu, Surface acoustic waves in graphene structures: Response to ambient humidity, SENSORS, 2010 IEEE, 2010, pp. 785–788.

84 F. Lan, L. Liang, Y. Zhang, L. Li, N. Ren, M. Yan, S. Ge and J. Yu, *ACS Appl. Mater. Interfaces*, 2017, **9**, 37839–37847.

85 M. Govindasamy, V. Mani, S.-M. Chen, T. Maiyalagan, S. Selvaraj, T.-W. Chen, S.-Y. Lee and W.-H. Chang, *RSC Adv.*, 2017, **7**, 33043–33051.

86 S. Kumar, P. Bhushan and S. Bhattacharya, *RSC Adv.*, 2017, **7**, 37568–37577.

87 J. Oh, J. S. Lee, J. Jun, S. G. Kim and J. Jang, *ACS Appl. Mater. Interfaces*, 2017, **9**, 39526–39533.

88 W. Cheng, P. Liu, M. Zhang, J. Huang, F. Cheng and L. Wang, *RSC Adv.*, 2017, **7**, 47781–47788.

89 H. Peng, L. Zhang, Z. Cai, Y. Wu, N. Chen, C. Gu, Y. Chen, X. Lin, X. Xia and A. Liu, *RSC Adv.*, 2017, 7, 36728–36734.

90 B. Han, Y.-L. Zhang, L. Zhu, X.-H. Chen, Z.-C. Ma, X.-L. Zhang, J.-N. Wang, W. Wang, Y.-Q. Liu, Q.-D. Chen and H.-B. Sun, *Sens. Actuators, B*, 2018, **270**, 500–507.

1220 | *J. Mater. Chem. C,* 2020, **8**, 1198–1224

This journal is © The Royal Society of Chemistry 2020

91 S. K. Basiruddin and S. K. Swain, *Mater. Sci. Eng., C*, 2016, **58**, 103–109.

92 F. Liu, Y. H. Kim, D. S. Cheon and T. S. Seo, *Sens. Actuators, B*, 2013, **186**, 252–257.

93 C. Reiner-Rozman, C. Kotlowski and W. Knoll, *Biosensors*, 2016, **6**, 17.

94 J. Xu, Y. Lin, Y. Hu, S. Xie and J. Lin, *A reduced graphene oxide-based fluorescence resonance energy transfer sensor for highly sensitive detection of trypsin*, International Conference on Photonics and Imaging in Biology and Medicine, Suzhou, Optical Society of America, Suzhou, p. W3A.129.

95 G. Zhao, L. Yang, S. Wu, H. Zhao, E. Tang and C.-P. Li, *Biosens. Bioelectron.*, 2017, **91**, 863–869.

96 H. G. Sudibya, Q. He, H. Zhang and P. Chen, *ACS Nano*, 2011, **5**, 1990–1994.

97 J. W. Park, S. J. Park, O. S. Kwon, C. Lee and J. Jang, *Analyst*, 2014, **139**, 3852–3855.

98 A. M. Şenol, Y. Onganer and K. Meral, *Sens. Actuators, B*, 2017, **239**, 343–351.

99 V. Van Cat, N. X. Dinh, L. T. Tam, N. V. Quy, V. N. Phan and A.-T. Le, *Mater. Today Commun.*, 2019, **21**, 100639.

100 J. Yu, Y. Ma, C. Yang, H. Zhang, L. Liu, J. Su and Y. Gao, *Sens. Actuators, B*, 2018, **254**, 182–188.

101 T. K. Naqvi, A. K. Srivastava, M. M. Kulkarni, A. M. Siddiqui and P. K. Dwivedi, *Appl. Surf. Sci.*, 2019, **478**, 887–895.

102 T. Y. Choi, B.-U. Hwang, B.-Y. Kim, T. Q. Trung, Y. H. Nam, D.-N. Kim, K. Eom and N.-E. Lee, *ACS Appl. Mater. Interfaces*, 2017, **9**, 18022–18030.

103 S. Zhao, L. Guo, J. Li, N. Li, G. Zhang, Y. Gao, J. Li, D. Cao, W. Wang, Y. Jin, R. Sun and C.-P. Wong, *Small*, 2017, **13**, 1700944.

104 S. J. Kim, W. Song, Y. Yi, B. K. Min, S. Mondal, K.-S. An and C.-G. Choi, *ACS Appl. Mater. Interfaces*, 2018, **10**, 3921–3928.

105 B. Saha, S. Baek and J. Lee, *ACS Appl. Mater. Interfaces*, 2017, **9**, 4658–4666.

106 J. An, T.-S. D. Le, Y. Huang, Z. Zhan, Y. Li, L. Zheng, W. Huang, G. Sun and Y.-J. Kim, *ACS Appl. Mater. Interfaces*, 2017, **9**, 44593–44601.

107 T. M. Perfecto, C. A. Zito, T. Mazon and D. P. Volanti, *J. Mater. Chem. C*, 2018, **6**, 2822–2829.

108 C. S. Yeo, H. Kim, T. Lim, H. J. Kim, S. Cho, K. R. Cho, Y. S. Kim, M. K. Shin, J. Yoo, S. Ju and S. Y. Park, *J. Mater. Chem. C*, 2017, **5**, 12825–12832.

109 A. V. Singhal, H. Charaya and I. Lahiri, *Crit. Rev. Solid State Mater. Sci.*, 2017, **42**, 499–526.

110 S. Mao, H. Pu, J. Chang, X. Sui, G. Zhou, R. Ren, Y. Chen and J. Chen, *Environ. Sci.: Nano*, 2017, **4**, 856–863.

111 C. Zhu, X. Wang, X. Shi, F. Yang, G. Meng, Q. Xiong, Y. Ke, H. Wang, Y. Lu and N. Wu, *ACS Appl. Mater. Interfaces*, 2017, **9**, 39618–39625.

112 S. Park, J. An, I. Jung, R. D. Piner, S. J. An, X. Li, A. Velamakanni and R. S. Ruoff, *Nano Lett.*, 2009, **9**, 1593–1597.

113 S. Y. Jeong, S. H. Kim, J. T. Han, H. J. Jeong, S. Y. Jeong and G.-W. Lee, *Adv. Funct. Mater.*, 2012, **22**, 3307–3314.

114 T. Hoshide, Y. Zheng, J. Hou, Z. Wang, Q. Li, Z. Zhao, R. Ma, T. Sasaki and F. Geng, *Nano Lett.*, 2017, **17**, 3543–3549.

115 T. Meng, F. Yi, H. Cheng, J. Hao, D. Shu, S. Zhao, C. He, X. Song and F. Zhang, *ACS Appl. Mater. Interfaces*, 2017, **9**, 42883–42892.

116 Z. Ma, X. Zhou, W. Deng, D. Lei and Z. Liu, *ACS Appl. Mater. Interfaces*, 2018, **10**, 3634–3643.

117 H. Xiao, J. P. Pender, M. A. Meece-Rayle, J. P. de Souza, K. C. Klavetter, H. Ha, J. Lin, A. Heller, C. J. Ellison and C. B. Mullins, *ACS Appl. Mater. Interfaces*, 2017, **9**, 22641–22651.

118 H. Qi, L. Cao, J. Li, J. Huang, Z. Xu, Y. Cheng, X. Kong and K. Yanagisawa, *ACS Appl. Mater. Interfaces*, 2016, **8**, 35253–35263.

119 J.-S. Park, J.-H. Jo, H. Yashiro, S.-S. Kim, S.-J. Kim, Y.-K. Sun and S.-T. Myung, *ACS Appl. Mater. Interfaces*, 2017, **9**, 25941–25951.

120 M. S. A. Sher Shah, A. R. Park, A. Rauf, S. H. Hong, Y. Choi, J. Park, J. Kim, W.-J. Kim and P. J. Yoo, *RSC Adv.*, 2017, **7**, 3125–3135.

121 G. Li, M. Jing, Z. Chen, B. He, M. Zhou and Z. Hou, *RSC Adv.*, 2017, **7**, 10376–10384.

122 Y.-J. Zhang, J. Qu, S.-M. Hao, W. Chang, Q.-Y. Ji and Z.-Z. Yu, *ACS Appl. Mater. Interfaces*, 2017, **9**, 41878–41886.

123 T. Li, A. Qin, L. Yang, J. Chen, Q. Wang, D. Zhang and H. Yang, *ACS Appl. Mater. Interfaces*, 2017, **9**, 19900–19907.

124 J. Cao, C. Chen, Q. Zhao, N. Zhang, Q. Lu, X. Wang, Z. Niu and J. Chen, *Adv. Mater.*, 2016, **28**, 9629–9636.

125 J. Zhao, Y.-Z. Zhang, F. Zhang, H. Liang, F. Ming, H. N. Alshareef and Z. Gao, *Adv. Energy Mater.*, 2019, **9**, 1803215.

126 J.-H. Kim, Y. H. Jung, J. H. Yun, P. Ragupathy and D. K. Kim, *Small*, 2018, **14**, 1702605.

127 J. Li, X. Li, D. Xiong, Y. Hao, H. Kou, W. Liu, D. Li and Z. Niu, *RSC Adv.*, 2017, **7**, 55060–55066.

128 J. Smajic, A. Alazmi, N. Batra, T. Palanisamy, D. H. Anjum and P. M. F. J. Costa, *Small*, 2018, **14**, 1803584.

129 Y. Zhang, G. Wang, L. Wang, L. Tang, M. Zhu, C. Wu, S.-X. Dou and M. Wu, *Nano Lett.*, 2019, **19**, 2575–2582.

130 W.-H. Khoh and J.-D. Hong, *Colloids Surf., A*, 2013, **436**, 104–112.

131 N.-L. Wu, S.-Y. Wang, C.-Y. Han, D.-S. Wu and L.-R. Shiue, *J. Power Sources*, 2003, **113**, 173–178.

132 V. Augustyn, P. Simon and B. Dunn, *Energy Environ. Sci.*, 2014, **7**, 1597–1614.

133 I. Shown, A. Ganguly, L.-C. Chen and K.-H. Chen, *Energy Sci. Eng.*, 2015, **3**, 2–26.

134 F.-H. Kuok, H.-H. Chien, C.-C. Lee, Y.-C. Hao, I.-S. Yu, C.-C. Hsu, I. C. Cheng and J.-Z. Chen, *RSC Adv.*, 2018, **8**, 2851–2857.

135 M. Huang, L. Wang, S. Chen, L. Kang, Z. Lei, F. Shi, H. Xu and Z.-H. Liu, *RSC Adv.*, 2017, **7**, 10092–10099.

136 R. Kumar, R. K. Singh, A. R. Vaz, R. Savu and S. A. Moshkalev, *ACS Appl. Mater. Interfaces*, 2017, **9**, 8880–8890.

137 H. Ma, H. Geng, B. Yao, M. Wu, C. Li, M. Zhang, F. Chi and L. Qu, *ACS Nano*, 2019, **13**, 9161–9170.

138 Á. Pérez del Pino, A. Martínez Villarroya, A. Chuquitarqui, C. Logofatu, D. Tonti and E. György, *J. Mater. Chem. A*, 2018, **6**, 16074–16086.

139 J. Gao, C. Shao, S. Shao, C. Bai, U. R. Khalil, Y. Zhao, L. Jiang and L. Qu, *ACS Nano*, 2019, **13**, 7463–7470.

140 G. Bhattacharya, G. Kandasamy, N. Soin, R. K. Upadhyay, S. Deshmukh, D. Maity, J. McLaughlin and S. S. Roy, *RSC Adv.*, 2017, **7**, 327–335.

141 S. Sarkar, P. Howli, B. Das, N. S. Das, M. Samanta, G. C. Das and K. K. Chattopadhyay, *ACS Appl. Mater. Interfaces*, 2017, **9**, 22652–22664.

142 X. Mu, J. Du, Y. Zhang, Z. Liang, H. Wang, B. Huang, J. Zhou, X. Pan, Z. Zhang and E. Xie, *ACS Appl. Mater. Interfaces*, 2017, **9**, 35775–35784.

143 L. Xu, Y. Li, M. Jia, Q. Zhao, X. Jin and C. Yao, *RSC Adv.*, 2017, **7**, 45066–45074.

144 J. Chang, H. Xu, J. Sun and L. Gao, *J. Mater. Chem.*, 2012, **22**, 11146–11150.

145 P. Bhattacharya, T. Joo, M. Kota and H. S. Park, *Ceram. Int.*, 2018, **44**, 980–987.

146 K. Wang, X. Dong, C. Zhao, X. Qian and Y. Xu, *Electrochim. Acta*, 2015, **152**, 433–442.

147 J. Sun, C. Wu, X. Sun, H. Hu, C. Zhi, L. Hou and C. Yuan, *J. Mater. Chem. A*, 2017, **5**, 9443–9464.

148 W. Quan, Z. L. Tang, S. T. Wang, Y. Hong and Z. T. Zhang, *Chem. Commun.*, 2016, **52**, 3694–3696.

149 H. K. Hassan, N. F. Atta, M. M. Hamed, A. Galal and T. Jacob, *RSC Adv.*, 2017, **7**, 11286–11296.

150 J. R. Rani, R. Thangavel, S.-I. Oh, J. M. Woo, N. Chandra Das, S.-Y. Kim, Y.-S. Lee and J.-H. Jang, *ACS Appl. Mater. Interfaces*, 2017, **9**, 22398–22407.

151 L. He and S. C. Tjong, *RSC Adv.*, 2017, **7**, 2058–2065.

152 B. Ahmed, A. K. Ojha, F. Hirsch, I. Fischer, D. Patrice and A. Materny, *RSC Adv.*, 2017, **7**, 13985–13996.

153 B. D. Ossonon and D. Bélanger, *RSC Adv.*, 2017, **7**, 27224–27234.

154 X. Wang, H. Tian, M. A. Mohammad, C. Li, C. Wu, Y. Yang and T.-L. Ren, *Nat. Commun.*, 2015, **6**, 7767.

155 B. Tang, G. Ji, Z. Wang, H. Chen, X. Li, H. Yu, S. Li and H. Liu, *RSC Adv.*, 2017, **7**, 45280–45286.

156 P. Dong, M.-T. F. Rodrigues, J. Zhang, R. S. Borges, K. Kalaga, A. L. M. Reddy, G. G. Silva, P. M. Ajayan and J. Lou, *Nano Energy*, 2017, **42**, 181–186.

157 X.-X. Yu, H. Yin, H.-X. Li, H. Zhao, C. Li and M.-Q. Zhu, *J. Mater. Chem. C*, 2018, **6**, 630–636.

158 S. R. Gollu, R. Sharma, G. Srinivas, S. Kundu and D. Gupta, *Org. Electron.*, 2016, **29**, 79–87.

159 S. Lee, J.-S. Yeo, J.-M. Yun and D.-Y. Kim, *Opt. Mater. Express*, 2017, **7**, 2487–2495.

160 P. C. Mahakul, K. Sa, B. V. R. S. Subramanyam and P. Mahanandia, *Mater. Chem. Phys.*, 2019, **226**, 113–117.

161 D. C. Tiwari, S. K. Dwivedi, P. Dipak and T. Chandel, *AIP Conf. Proc.*, 2018, **1953**, 100065.

162 S. J. Lee, J.-Y. Kim, A. R. b. Mohd Yusoff and J. Jang, *RSC Adv.*, 2015, **5**, 23892–23899.

163 M. M. Tavakoli, R. Tavakoli, Z. Nourbakhsh, A. Waleed, U. S. Virk and Z. Fan, *Adv. Mater. Interfaces*, 2016, **3**, 1500790.

164 E. Jokar, Z. Y. Huang, S. Narra, C.-Y. Wang, V. Kattoor, C.-C. Chung and E. W.-G. Diau, *Adv. Energy Mater.*, 2018, **8**, 1701640.

165 S. S. Mali, C. S. Shim, H. Kim and C. K. Hong, *J. Mater. Chem. A*, 2016, **4**, 12158–12169.

166 L. Ding, H. Tao, C. Zhang, J. Li, W. Zhang, J. Wang and J. Xue, *Mater. Sci. Semicond. Process.*, 2020, **107**, 104798.

167 J. V. Milić, N. Arora, M. I. Dar, S. M. Zakeeruddin and M. Grätzel, *Adv. Mater. Interfaces*, 2018, **5**, 1800416.

168 R. Liu, R. Qiu, T. Zou, C. Liu, J. Chen, Q. Dai, S. Zhang and H. Zhou, *Nanotechnology*, 2018, **30**, 075202.

169 X. Jiang, Z. Wang, W. Han, Q. Liu, S. Lu, Y. Wen, J. Hou, F. Huang, S. Peng, D. He and G. Cao, *Appl. Surf. Sci.*, 2017, **407**, 398–404.

170 L. J. Larsen, C. J. Shearer, A. V. Ellis and J. G. Shapter, *J. Phys. Chem. C*, 2016, **120**, 15648–15656.

171 M. Han, B. D. Ryu, J.-H. Hyung, N. Han, Y. J. Park, K. B. Ko, K. K. Kang, T. V. Cuong and C.-H. Hong, *Mater. Sci. Semicond. Process.*, 2017, **59**, 45–49.

172 S. Yavuz and P. R. Bandaru, Ag nanowire coated reduced graphene oxide/n-silicon Schottky junction based solar cell, 2016 IEEE Conference on Technologies for Sustainability (SusTech), 2016, pp. 265–269.

173 C. V. V. M. Gopi, S. Singh, A. Eswar Reddy and H.-J. Kim, *ACS Appl. Mater. Interfaces*, 2018, **10**, 10036–10042.

174 B. Yuan, Q. Gao, X. Zhang, L. Duan, L. Chen, Z. Mao, X. Li and W. Lü, *Electrochim. Acta*, 2018, **277**, 50–58.

175 K. Xiong, W. Nie, P. Yu, L. Zhu and X. Xiao, *Mater. Lett.*, 2017, **204**, 69–72.

176 F. Du, X. Zuo, Q. Yang, B. Yang, G. Li, H. Tang, H. Zhang, M. Wu and Y. Ma, *Sol. Energy Mater. Sol. Cells*, 2016, **149**, 9–14.

177 A. Sarkar, A. K. Chakraborty and S. Bera, *Sol. Energy Mater. Sol. Cells*, 2018, **182**, 314–320.

178 M. F. Abdullah and A. M. Hashim, *J. Mater. Sci.*, 2019, **54**, 911–948.

179 E. Singh and H. S. Nalwa, *Sci. Adv. Mater.*, 2015, **7**, 1863–1912.

180 E. Singh and H. S. Nalwa, *J. Nanosci. Nanotechnol.*, 2015, **15**, 6237–6278.

181 M. Javadi, M. Gholami and Y. Abdi, *J. Mater. Chem. C*, 2018, **6**, 8444–8452.

182 G. Zhou, J. Chang, S. Cui, H. Pu, Z. Wen and J. Chen, *ACS Appl. Mater. Interfaces*, 2014, **6**, 19235–19241.

183 S. Lim, B. Kang, D. Kwak, W. H. Lee, J. A. Lim and K. Cho, *J. Phys. Chem. C*, 2012, **116**, 7520–7525.

184 F. J. Romero, A. Toral-Lopez, A. Ohata, D. P. Morales, F. G. Ruiz, A. Godoy and N. Rodriguez, *Nanomaterials*, 2019, **9**, 897.

185 J. T. Robinson, M. Zalalutdinov, J. W. Baldwin, E. S. Snow, Z. Wei, P. Sheehan and B. H. Houston, *Nano Lett.*, 2008, **8**, 3441–3445.

186 X. Zhu, S. Wang, C. Li, Y. Zhang, W. Fang, Y. Lu, C. Guo, R. Wang, Y. Zhang, W. Xu, X. Li and T.-C. Poon, *Opt. Mater. Express*, 2019, **9**, 4497–4505.

187 V. Dua, S. P. Surwade, S. Ammu, S. R. Agnihotra, S. Jain, K. E. Roberts, S. Park, R. S. Ruoff and S. K. Manohar, *Angew. Chem., Int. Ed.*, 2010, **49**, 2154–2157.

188 Y. Su, J. Du, D. Sun, C. Liu and H. Cheng, *Nano Res.*, 2013, **6**, 842–852.

189 B. W. An, K. Kim, M. Kim, S.-Y. Kim, S.-H. Hur and J.-U. Park, *Small*, 2015, **11**, 2263–2268.

190 J. H. Kim, W. S. Chang, D. Kim, J. R. Yang, J. T. Han, G.-W. Lee, J. T. Kim and S. K. Seol, *Adv. Mater.*, 2015, **27**, 157–161.

191 S. Fang, D. Huang, R. Lv, Y. Bai, Z.-H. Huang, J. Gu and F. Kang, *RSC Adv.*, 2017, **7**, 25773–25779.

192 C. Zhang, B. Wang, J. Xiang, C. Su, C. Mu, F. Wen and Z. Liu, *ACS Appl. Mater. Interfaces*, 2017, **9**, 28868–28875.

193 M. Hashemi, M. Omidi, B. Muralidharan, H. Smyth, M. A. Mohagheghi, J. Mohammadi and T. E. Milner, *ACS Appl. Mater. Interfaces*, 2017, **9**, 32607–32620.

194 J. Feng, Y. Hou, Y. Wang and L. Li, *ACS Appl. Mater. Interfaces*, 2017, **9**, 14103–14111.

195 H. Pan, M. Xu, Q. Qi and X. Liu, *RSC Adv.*, 2017, **7**, 43831–43838.

196 J. Luo, Y. Zuo, P. Shen, Z. Yan and K. Zhang, *RSC Adv.*, 2017, **7**, 36433–36443.

197 L. He, Y. Zhao, L. Xing, P. Liu, Z. Wang, Y. Zhang, Y. Wang and Y. Du, *RSC Adv.*, 2018, **8**, 2971–2977.

198 S. Kim, J.-S. Oh, M.-G. Kim, W. Jang, M. Wang, Y. Kim, H. W. Seo, Y. C. Kim, J.-H. Lee, Y. Lee and J.-D. Nam, *ACS Appl. Mater. Interfaces*, 2014, **6**, 17647–17653.

199 A. P. Singh, M. Mishra, D. P. Hashim, T. N. Narayanan, M. G. Hahm, P. Kumar, J. Dwivedi, G. Kedawat, A. Gupta, B. P. Singh, A. Chandra, R. Vajtai, S. K. Dhawan, P. M. Ajayan and B. K. Gupta, *Carbon*, 2015, **85**, 79–88.

200 J. Chen, J. Wu, H. Ge, D. Zhao, C. Liu and X. Hong, *Composites, Part A*, 2016, **82**, 141–150.

201 J. Prasad, A. K. Singh, K. K. Haldar, V. Gupta and K. Singh, *J. Alloys Compd.*, 2019, **788**, 861–872.

202 A. P. Singh, P. Garg, F. Alam, K. Singh, R. B. Mathur, R. P. Tandon, A. Chandra and S. K. Dhawan, *Carbon*, 2012, **50**, 3868–3875.

203 J. Prasad, A. K. Singh, M. Tomar, V. Gupta and K. Singh, *J. Mater. Sci.: Mater. Electron.*, 2019, **30**, 18666–18677.

204 J. Prasad, A. K. Singh, J. Shah, R. K. Kotnala and K. Singh, *Mater. Res. Express*, 2018, **5**, 055028.

205 G. Sobon, J. Sotor, J. Jagiello, R. Kozinski, M. Zdrojek, M. Holdynski, P. Paletko, J. Boguslawski, L. Lipinska and K. M. Abramski, *Opt. Express*, 2012, **20**, 19463–19473.

206 Z.-D. Chen, Y.-G. Wang, L. Li, R.-D. Lv, L.-L. Wei, S.-C. Liu, J. Wang and X. Wang, *Chin. Phys. B*, 2018, **27**, 084206.

207 H. Ahmad, S. Soltani, K. Thambiratnam, M. Yasin and Z. C. Tiu, *Opt. Fiber Technol.*, 2019, **50**, 177–182.

208 J. Mohanraj, V. Velmurugan and S. Sivabalan, *Opto-Electron. Rev.*, 2019, **27**, 18–24.

209 V. Ramar and K. Balasubramanian, *Appl. Phys. A: Mater. Sci. Process.*, 2018, **124**, 779.

210 S.-D. Pan, L. Cui, J.-Q. Liu, B. Teng, J.-H. Liu and X.-H. Ge, *Opt. Mater.*, 2014, **38**, 42–45.

211 G. Sobon, J. Sotor, J. Jagiello, R. Kozinski, K. Librant, M. Zdrojek, L. Lipinska and K. M. Abramski, *Appl. Phys. Lett.*, 2012, **101**, 241106.

212 X. Fang, L. Jiao, R. Zhang and H.-L. Jiang, *ACS Appl. Mater. Interfaces*, 2017, **9**, 23852–23858.

213 T. He, X. Wang, H. Wu, H. Xue, P. Xue, J. Ma, M. Tan, S. He, R. Shen, L. Yi, Y. Zhang and J. Xiang, *ACS Appl. Mater. Interfaces*, 2017, **9**, 22490–22501.

214 G. D. Park, J. H. Kim, S.-K. Park and Y. C. Kang, *ACS Appl. Mater. Interfaces*, 2017, **9**, 10673–10683.

215 Y. Li, Y. Chen, A. Nie, A. Lu, R. J. Jacob, T. Gao, J. Song, J. Dai, J. Wan, G. Pastel, M. R. Zachariah, R. S. Yassar and L. Hu, *Adv. Energy Mater.*, 2017, **7**, 1601783.

216 P. Yu, L. Wang, Y. Xie, C. Tian, F. Sun, J. Ma, M. Tong, W. Zhou, J. Li and H. Fu, *Small*, 2018, **14**, 1801717.

217 Y. Hu, T. Mei, J. Li, J. Wang and X. Wang, *RSC Adv.*, 2017, **7**, 29909–29915.

218 W. Wang, X. Huang, M. Lai and C. Lu, *RSC Adv.*, 2017, **7**, 10517–10523.

219 Y. Tang, X. Liu, C. Ma, M. Zhou, P. Huo, L. Yu, J. Pan, W. Shi and Y. Yan, *New J. Chem.*, 2015, **39**, 5150–5160.

220 Z. Wan and J. Wang, *J. Hazard. Mater.*, 2017, **324**, 653–664.

221 L. Lin, H. Wang and P. Xu, *Chem. Eng. J.*, 2017, **310**, 389–398.

222 Y. Oz, A. Barras, R. Sanyal, R. Boukherroub, S. Szunerits and A. Sanyal, *ACS Appl. Mater. Interfaces*, 2017, **9**, 34194–34203.

223 L. Shao, R. Zhang, J. Lu, C. Zhao, X. Deng and Y. Wu, *ACS Appl. Mater. Interfaces*, 2017, **9**, 1226–1236.

224 Y. Yang, L. Zhu, F. Xia, B. Gong, A. Xie, S. Li, F. Huang, S. Wang, Y. Shen and D. T. Weaver, *RSC Adv.*, 2017, **7**, 2415–2425.

225 B. Khezri, S. M. Beladi Mousavi, L. Krejčová, Z. Heger, Z. Sofer and M. Pumera, *Adv. Funct. Mater.*, 2019, **29**, 1806696.

226 M. A. Ali, C. Singh, S. Srivastava, P. Admane, V. V. Agrawal, G. Sumana, R. John, A. Panda, L. Dong and B. D. Malhotra, *RSC Adv.*, 2017, **7**, 35982–35991.

227 J. A. Tyson, V. Mirabello, D. G. Calatayud, H. Ge, G. Kociok-Köhn, S. W. Botchway, D. G. Pantoş and S. I. Pascu, *Adv. Funct. Mater.*, 2016, **26**, 5641–5657.

228 S. K. S. Patel, S. H. Choi, Y. C. Kang and J.-K. Lee, *ACS Appl. Mater. Interfaces*, 2017, **9**, 2213–2222.

229 K. Xiong, T. Wu, Q. Fan, L. Chen and M. Yan, *ACS Appl. Mater. Interfaces*, 2017, **9**, 44356–44368.

230 W. Ma, F. Zhang, L. Li, S. Chen, L. Qi, H. Liu and Y. Bai, *ACS Appl. Mater. Interfaces*, 2016, **8**, 35099–35105.

231 S. H. Lee, H. B. Lee, Y. Kim, J. R. Jeong, M. H. Lee and K. Kang, *Nano Lett.*, 2018, **18**, 7421–7427.

232 F. S. Awad, K. M. AbouZeid, W. M. A. El-Maaty, A. M. El-Wakil and M. S. El-Shall, *ACS Appl. Mater. Interfaces*, 2017, **9**, 34230–34242.

233 S. K. Ray, C. Majumder and P. Saha, *RSC Adv.*, 2017, **7**, 21768–21779.

234 Y. Zhang, X. Yan, Y. Yan, D. Chen, L. Huang, J. Zhang, Y. Ke and S. Tan, *RSC Adv.*, 2018, **8**, 4239–4248.

235 J. Liu, J. Ke, D. Li, H. Sun, P. Liang, X. Duan, W. Tian, M. O. Tadé, S. Liu and S. Wang, *ACS Appl. Mater. Interfaces*, 2017, **9**, 11678–11688.

236 Z. Chen, J. Zhang, K. Han, C. Yang, X. Jiang, D. Fu, Q. Li and Y. Wang, *RSC Adv.*, 2017, **7**, 31075–31084.

237 Q. Wang, C. Aubry, Y. Chen, H. Song and L. Zou, *ACS Appl. Mater. Interfaces*, 2017, **9**, 22509–22517.

238 W. Jia, B. Tang and P. Wu, *ACS Appl. Mater. Interfaces*, 2017, **9**, 22620–22627.

239 J. Zhu, J. Wang, A. A. Uliana, M. Tian, Y. Zhang, Y. Zhang, A. Volodin, K. Simoens, S. Yuan, J. Li, J. Lin, K. Bernaerts and B. Van der Bruggen, *ACS Appl. Mater. Interfaces*, 2017, **9**, 28990–29001.

240 M. B. McDonald, J. P. Bruce, K. McEleney and M. S. Freund, *ChemSusChem*, 2015, **8**, 2645–2654.

241 J. Yang, Y. Pang, W. Huang, S. K. Shaw, J. Schiffbauer, M. A. Pillers, X. Mu, S. Luo, T. Zhang, Y. Huang, G. Li, S. Ptasinska, M. Lieberman and T. Luo, *ACS Nano*, 2017, **11**, 5510–5518.

242 S. Colonna, R. A. Pérez-Camargo, H. Chen, G. Liu, D. Wang, A. J. Müller, G. Saracco and A. Fina, *Macromolecules*, 2017, **50**, 9380–9393.

243 G. Yao, T. Duan, M. An, H. Xu, F. Tian and Z. Wang, *RSC Adv.*, 2017, **7**, 21918–21925.

244 A. Gholampour, M. Valizadeh Kiamahalleh, D. N. H. Tran, T. Ozbakkaloglu and D. Losic, *ACS Appl. Mater. Interfaces*, 2017, **9**, 43275–43286.

245 C. Phrompet, C. Sriwong and C. Ruttanapun, *Composites, Part B*, 2019, **175**, 107128.

246 P. Bhawal, S. Ganguly, T. K. Das, S. Mondal, S. Choudhury and N. C. Das, *Composites, Part B*, 2018, **134**, 46–60.

247 Y. F. Sun, T. S. Zhou, P. W. Gao, M. Chen, H. W. Liu and Y. Xun, *Strength Mater.*, 2019, **51**, 601–608.

248 Y. Sun, M. Chen, P. Gao, T. Zhou, H. Liu and Y. Xun, *Adv. Mech. Eng.*, 2019, **11**, 1–11.

249 S. K. Tiwari, K. Verma, P. Saren, R. Oraon, A. De Adhikari, G. C. Nayak and V. Kumar, *RSC Adv.*, 2017, **7**, 22145–22155.

250 N. Song, X. Hou, L. Chen, S. Cui, L. Shi and P. Ding, *ACS Appl. Mater. Interfaces*, 2017, **9**, 17914–17922.

251 A. Hazarika, B. K. Deka, D. Kim, H. D. Roh, Y.-B. Park and H. W. Park, *ACS Appl. Mater. Interfaces*, 2017, **9**, 36311–36319.

252 L. Dong, C. Hu, L. Song, X. Huang, N. Chen and L. Qu, *Adv. Funct. Mater.*, 2016, **26**, 1470–1476.

253 Y.-K. Xiao, W.-F. Ji, K.-S. Chang, K.-T. Hsu, J.-M. Yeh and W.-R. Liu, *RSC Adv.*, 2017, **7**, 33829–33836.

254 X. Luo, S. Yuan, X. Pan, C. Zhang, S. Du and Y. Liu, *ACS Appl. Mater. Interfaces*, 2017, **9**, 18263–18275.

255 J. Zhao, Y. Li, Y. Wang, J. Mao, Y. He and J. Luo, *RSC Adv.*, 2017, **7**, 1766–1770.

1224 | *J. Mater. Chem. C*, 2020, **8**, 1198–1224

This journal is © The Royal Society of Chemistry 2020